TiEMPO:Time-Dependent End-to-End Model for Post-process Optimization of the DESHIMA Spectrometer

Esmee Huijten

Delft University of Technology

TU Delft Delft University of Technology

Challenge the future

TiEMPO: Time-Dependent End-to-End Model for Post-process Optimization of the DESHIMA Spectrometer

by

Esmee Huijten

in partial fulfillment of the requirements for the degree of

Bachelor of Science
in Applied Physics and Applied Mathematics

at the Delft University of Technology,
to be defended publicly on the 6th of July 2020, 11:00

Supervisor:	Dr. A. Endo,	TU Delft
Thesis committee:	Dr. M. B. van Hoven,	TU Delft
	Dr. A. J. L. Adam,	TU Delft
	Prof. Dr. ir. A. W. Heemink,	TU Delft

This thesis is confidential and cannot be made public until 6 July 2020

Credits of the front page picture:
Starry sky: https://nl.freepik.com/vrije-foto-vectoren/achtergrond
Atacama Desert: Sven Peetoom, http://www.svenpeetoom.com/
Spectromenter chip: David J. Thoen

An electronic version of this thesis is available at http://repository.tudelft.nl/.

TU Delft Delft University of Technology

Abstract

Ultra-wideband submillimeter observations are crucial to study the process of star and galaxy formation and for characterizing cosmic dust in the interstellar medium. The Deep Spectroscopic High-redshift Mapper 2.0 (DESHIMA 2.0) will use an integrated superconducting spectrometer chip with a 220-440 GHz band coverage and a spectral resolution of $\frac{f}{\Delta f} = 500$, enabling submillimeter observations with an unprecedented instantaneous band coverage.

However, the octave bandwidth of DESHIMA 2.0 poses a challenge: the atmospheric transmission is highly nonlinear in the broad frequency window of DESHIMA 2.0, complicating the removal of atmosphere noise from the signal.

In this thesis, I present the Time-dependent End-to-end Model for Post-process Optimization (TiEMPO). TiEMPO provides realistic time-dependent simulations of high-redshift galaxy observations. It consists of the following components:
Galaxy model. A galaxy is modeled using a two-component modified blackbody spectrum as a template. The model outputs the flux density, which is converted to power spectral density using the frequency-dependent effective aperture area of the telescope.
Atmosphere model. TiEMPO makes use of atmosphere model ARIS, which models a spatially and dynamically varying atmosphere and outputs Extra Path Length [1]. TiEMPO converts this to precipitable water vapor using a relation that was found with the Smith-Weintraub value of the Extra Path Length and the ideal gas law.
Telescope beam. TiEMPO can be adapted to use any arbitrary beam shape for the near-field telescope beam. The far-field beam is modeled using the effective aperture area. Finally, the output of TiEMPO is given at multiple positions, enabling simulations of sky chopping and nodding in two directions.
Radiation transfer. A static model of the sensitivity of DESHIMA, determining the attenuation and the emission of the atmosphere and transmitting the signal through each component of the telescope and instrument.
Spectrometer chip. TiEMPO can adopt any filter transmission of the channels inside a spectrometer chip. In this work, they are approximated with Lorentzian curves. The photon and recombination noise are modeled with the NEP mentioned in [2], and the noise distribution is approximated with a normal distribution. The noise is incorporated with an integration over the filter response, treating photon-bunching over the wide bandwidth of DESHIMA 2.0 accurately.
Conversion to sky temperature. Finally, the power measured in the chip is related to the sky temperature with an interpolation made with a skydip simulation in the radiation transfer model.

We compare the first TiEMPO simulations to observation data by comparing the time signal, power spectral density and noise equivalent flux density. Apart from a small offset in the power spectral density, the simulation data closely resembles the observation data. TiEMPO allows us to test algorithms for atmosphere removal and galaxy detection, to study the effect of different weather conditions and to evaluate the performance of different observing techniques. TiEMPO is modular, making it usable for the original DESHIMA instrument and its successor DESHIMA 2.0. The use of TiEMPO can be extended to other spectrometers besides DESHIMA 2.0, like a grating spectrometer, and other telescopes, such as the promising 50m-aperture AtLAST/LST telescope [3] [4].

Contents

List of Symbols

Acronyms

ARIS	Astronomical Radio Interferometer Simulator
ASTE	Atacama Submillimeter Telescope Experiment
DESHIMA	Deep Spectroscopic High-Redshift Mapper
desim	(static) DESHIMA simulator
MKID	Microwave Kinetic Inductance Detector
SMG	Submillimeter-Bright Galaxy
TiEMPO	Time-dependent End-to-end Model for Post-process Optimization

Physics Constants

c	Speed of light	$299,792,458\,\mathrm{m\,s^{-1}}$
h	Planck's constant	$6.62607004 \cdot 10^{-34}\,\mathrm{m^2 kg\,s^{-1} Hz^{-1}}$
k_B	Boltzmann's constant	$1.38064852 \cdot 10^{-23}\,\mathrm{m^2 kg\,s^{-2} K^{-1}}$
R	Gas constant	$8.314462\,\mathrm{J\,mol^{-1} K^{-1}}$

Parameters

Δf	Bandwidth	Hz
Δ	Gap energy of a superconductor	eV
η	Transmission/efficiency	
λ	wavelength	m
Ω	solid angle	sr
ρ	density of molecules	$\mathrm{m^{-3}}$
A	Aperture area	$\mathrm{m^2}$
B_f	Spectral radiance	$\mathrm{W sr^{-1} m^{-2} Hz^{-1}}$
E	Energy	eV or J
e	Partial pressure of water vapor	mbar
EPL	Extra Path Length	m
f	Frequency	Hz
F_f	Flux density	$\mathrm{W m^{-2} Hz^{-1}}$
h	Height	m
L_1	Inner scale ARIS	m

L_2	Outer scale ARIS	m
N	number of molecules	mol
n	Number of photons	
NEP	Noise Equivalent Power	$\mathrm{WHz}^{-\frac{1}{2}}$
P	Power	W
psd	Power spectral density	WHz^{-1}
pwv	Precipitable water vapor	m
r	radius	m
S	Noise power spectral density	$\mathrm{Jy}^2\mathrm{Hz}^{-1}$
s	Displacement vector	m
T	(Sky) Temperature	K
t	time	s
V	Volume	m^3
x	Position	m
z	Redshift	

1

Introduction

Distant galaxies are a treasure of cosmic history. There is much left to be discovered about the way stars form and galaxies evolve, especially in the early Universe. As many distant galaxies go through an intense star formation phase, they are a likely source of many discoveries about star formation and galaxy evolution [5]. However, dusty star-forming galaxies are largely unexplored as observing them poses two main challenges: they are (almost) only detectable with submillimeter observations and their radiation covers a wide frequency spectrum, making it difficult to study these galaxies with a single telescope instrument.

First of all, star formation causes thick clouds of dust to form, hiding the galaxy inside it. Dust particles absorb optical and ultraviolet emission from stars, and re-radiate this light as infrared and submillimeter light (Figure 1.1). Hence, these galaxies are called optically faint Submillimeter-Bright Galaxies (SMGs). This explains why we require submillimeter observations to give an insight into how stars form and why the development of instruments capable of making these observations is crucial.

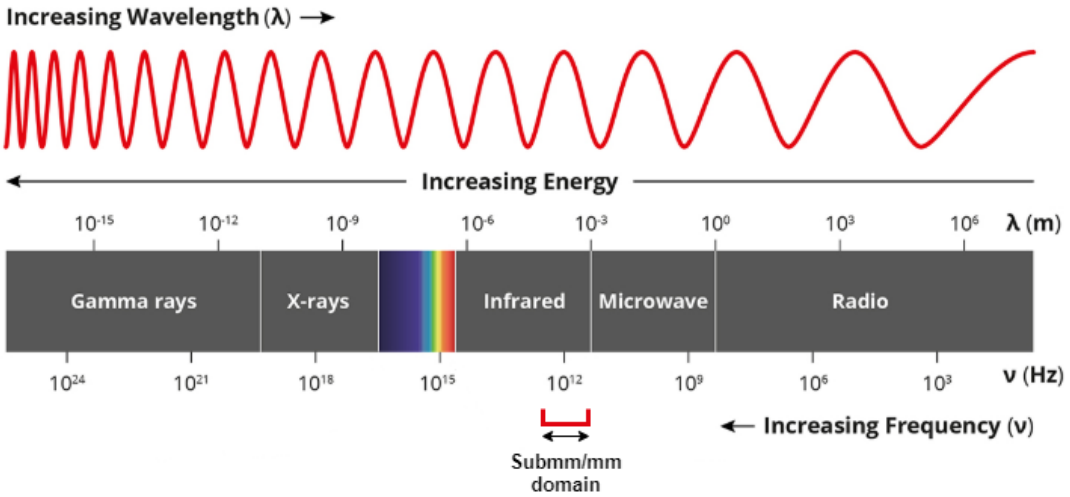

Figure 1.1: The electromagnetic spectrum with values of wavelengths and values of frequencies shown. The submm/mm domain is denoted at the bottom of the picture. The picture was made using [6].

Secondly, observations of SMGs are affected by a phenomenon called redshift. The further a galaxy is from Earth, the longer its light takes to travel to us. For SMGs, this typically takes billions of years. As space is expanding while light is traveling towards us, the wavelength of this light becomes larger (Figure 1.2). If the light were optical, the light would move more towards the red 'side' of the spectrum, explaining the name

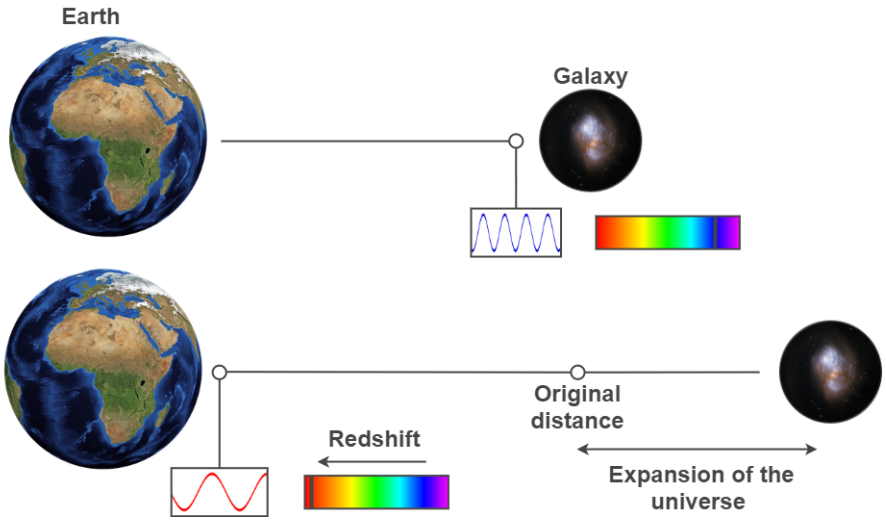

Figure 1.2: Illustration of the cosmological redshift. Blue light that comes from a galaxy travels a long time before it reaches Earth. In the mean time, space expands, increasing the wavelength of the light. This causes the light to be red by the time it reaches Earth, hence the name redshift. The figure is inspired by [9].

redshift. Redshift implies that the light we observe on Earth has a longer wavelength than the light originally emitted by the galaxy. The further away a galaxy is, the larger this effect. The redshift of SMGs is in the range of $1+z = \frac{f_{\text{emit}}}{f_{\text{observe}}} =$ 1-10, where $\frac{f_{\text{emit}}}{f_{\text{observe}}}$ denotes the ratio between the emitted and the observed frequencies [2]. Redshift is advantageous for our observations, as it allows us to relate a galaxy spectrum to its distance, and thus its age [1]. However, the large redshift range also complicates measurements, as we require a large bandwidth in order to observe galaxies at different distances from Earth. Coherent heterodyne receivers, which measure the power of the signal as well as the phase, currently only cover a bandwidth up to about 36 GHz, which is not enough to explore the range to which SMGs can be redshifted [7] [2]. Quasioptical spectrometers, like Fourier Transform spectrometers, have a wider bandwidth, but have large components, making it difficult to scale them up [8].

The Deep Spectroscopic High-Redshift Mapper (DESHIMA) overcomes these challenges [2] [10]. Whereas traditional telescope instruments, like quasioptical spectrometers, use large optical components to sort and detect the incoming light, DESHIMA uses a superconducting spectrometer chip. The spectrometer chip uses bandpass filters to sort the light of distant galaxies on frequency, and hence on age. DESHIMA is installed on the ASTE telescope in the Atacama Desert in Chile, where it has been operating since 2017 (Figure 1.3) [11]. The first light campaign of DESHIMA demonstrated atmospheric foreground photon-noise limited sensitivity. The experiments from the first light campaign showed that the DESHIMA technology has the potential of efficiently determining the redshift of a galaxy and making spectral maps of cosmic structures with unprecedented speed.

In 2020, the improved version of DESHIMA, DESHIMA 2.0, will be installed on ASTE [12]. DESHIMA 2.0 will have a 220-440 GHz band coverage and it will be the first spectrometer chip spanning an octave in bandwidth, enabling observations in a broad redshift range [12] [13]. Its optical efficiency and spectral resolution will be significantly increased compared to DESHIMA [13]. This instrument is very promising, but hardware is not the only thing needed to make DESHIMA 2.0 succeed. The observing strategy and the post-processing software plays a large role as well, because the atmosphere adds noise to the signal.

ASTE is a ground-based telescope, meaning that the atmosphere obscures the astronomic signal and adds extra foreground power before it arrives at the telescope. In the submillimeter domain, the atmosphere is opaque in some frequency intervals, caused mainly by water vapor [14]. The composition of the atmosphere changes with position and with time, causing an ever-changing opacity of the atmosphere during an observation. Furthermore, DESHIMA 2.0 will observe an octave bandwidth, so the atmospheric transmission is highly nonlinear as a function of the frequency (Figure 1.4). Because of this, removing the atmospheric noise from the signal and

[1] since light travels longer if it comes from a larger distance, light with a larger redshift is older

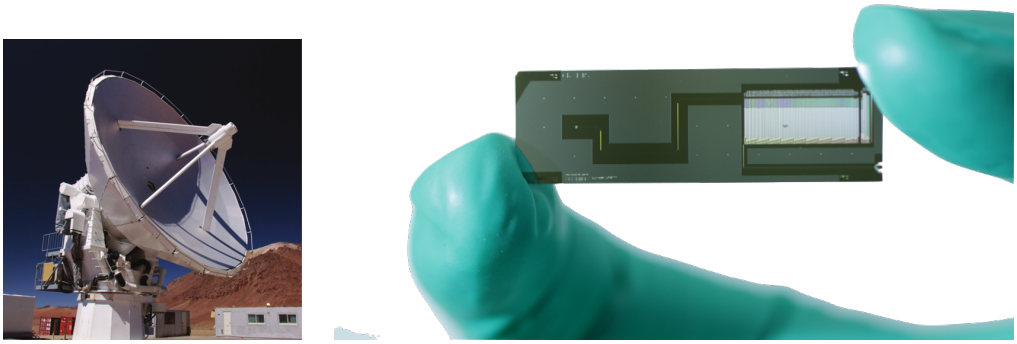

(a) (b)

Figure 1.3: (a) The Atacama Submillimeter Telescope Experiment (ASTE) with a 10 m dish, located in the Atacama Desert in Chile. The DESHIMA instrument is installed in ASTE. This picture is from the National Astronomical Observatory of Japan (NAOJ). (b) The integrated superconducting spectrometer chip of DESHIMA. This picture is from David Thoen (private communications).

calibrating the instrument output signal with the signal coming from the sky are significantly more complicated. Before this project, only static models existed, calculating the sensitivity of DESHIMA, but these models are not sufficient for this complicated problem. To be able to remove the atmospheric noise properly, we require a model that simulates the atmosphere spatially as well as dynamically. To make simulations as realistic as possible, it should be an end-to-end model of the whole process – from the galaxy emitting the light to the photodetection process in the spectrometer chip.

The goal of this project is to develop a model to produce realistic observation simulations of DESHIMA 2.0. To this end, we present the Time-dependent End-to-end Model for Post-process Optimization (TiEMPO) in this thesis. We explain the theory, assumptions and implementation of the model, and validate the output from the subcomponents as well as the entire system. The development of the TiEMPO model required a highly interdisciplinary approach, incorporating knowledge from astrophysics, solid-state physics, atmosphere science, quasioptics, and quantum optics. To give an idea, length scales in TiEMPO span over 30 orders of magnitude, from gigaparsecs ($\sim 10^{25}$ m – distance to galaxies), kilometers (atmosphere), to sub-millimeter ($\sim 10^{-5}$ m, length of superconducting filters). In the 'Early results of full simulations' chapter (Chapter 4), we show a few benchmark comparisons between the time-domain signal produced by TiEMPO and on-sky data taken by DESHIMA in 2017. The excellent agreement shows the potential of TiEMPO as a powerful tool for optimizing the software and observing strategies of DESHIMA 2.0.

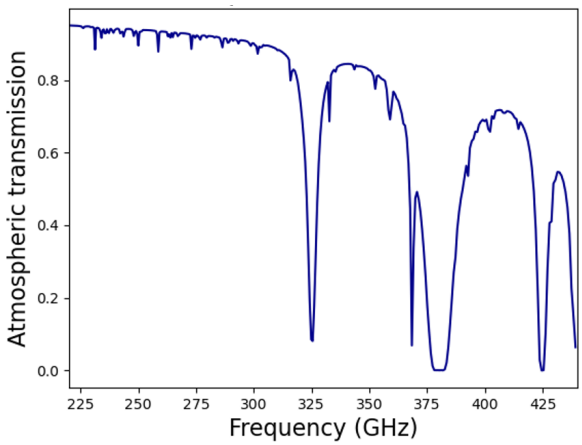

Figure 1.4: The atmospheric transmission plotted against the frequency in the domain of the DESHIMA 2.0 chip, showing that the atmospheric transmission is highly nonlinear in this domain. The data in this plot were obtained using [15] [16].

TiEMPO is modular, making it usable for the original DESHIMA instrument and its successor DESHIMA 2.0. It can even be used to test similar spectrometers, like a grating spectrometer, and on different telescopes, such as the promising 50m-aperture AtLAST/LST telescope [3] [4].

2

DESHIMA

The goal of the DESHIMA project is to observe SMGs and the interstellar medium, explore cosmic large-scale structures, and ultimately, make a 3D map of the Universe. This chapter explains how the DESHIMA instrument and the spectrometer chip work, discusses important observations made with DESHIMA, and shows the improvements that are made in the upgraded version of DESHIMA, DESHIMA 2.0.

2.1. DESHIMA INSTRUMENT

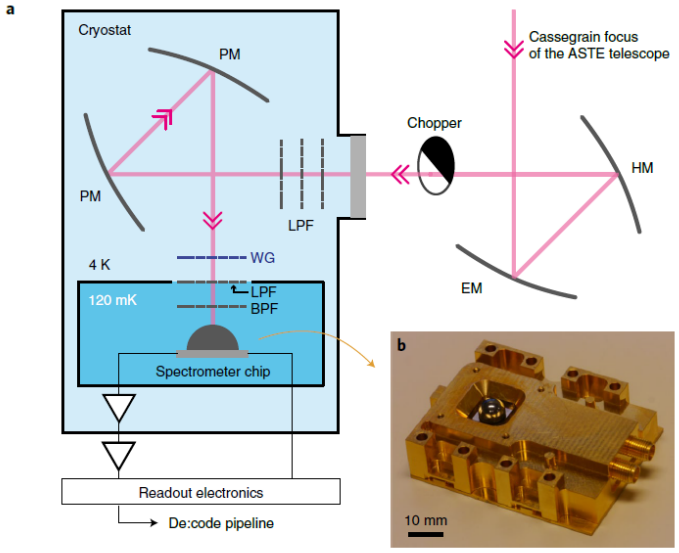

Figure 2.1: **a. Cryostat.** After entering the telescope, the signal is guided to the cryostat via an ellipsoidal tertiary mirror (EM) and a hyperbolic quaternary mirror (HM). Between these mirrors and the cryostat, the chopper wheel is located. The light then passes to the spectrometer chip through an optics tube, consisting of two parabolic mirrors (PM) and a wire grid (WG) polarizer, a stack of low-pass filters (LPF), and a bandpass filter (BPF). The readout electronics work with a frequency of 160 Hz. **b. Spectrometer chip.** The spectrometer chip in a copper housing. These pictures are taken from [2].

After the light has been focused by the telescope, it is guided into the DESHIMA instrument. A set of mirrors and other optical components lead the signal to the chip (Figure 2.1). The environment around the spectrometer

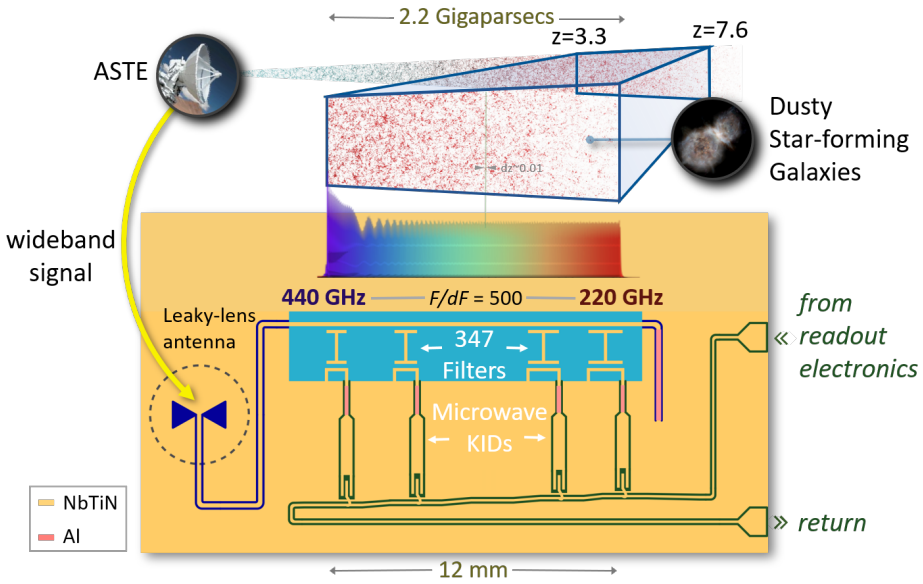

Figure 2.2: Illustration of the concept of the DESHIMA chip. It sorts the light on frequency, and thus on redshift and age. The DESHIMA 2.0 chip has 347 bandpass filters, with center frequencies ranging from 220 to 440 GHz. The signal enters the chip via the leaky-lens antenna and passes on to the filterbank. Each spectral channel contains a bandpass filter and a Microwave Kinetic Inductance Detector (MKID). The signal only creates resonance in the bandpass filter that matches the frequency of the signal. This filter gives power to the MKID in its channel. The MKID measures the power and finally, the power is absorbed in the aluminium section (colored pink in the image). The rest of the signal is absorbed by an aluminium strip at the end of the filterbank to prevent wave reflection causing standing waves in the sky signal line. All MKIDs are read out simultaneously with a readout signal (colored green in the image). This image is from Akira Endo (private communications).

chip is cooled down to 120 mK, to give the chip superconducting properties and suppress thermal noise.

2.2. Spectrometer chip

In Chapter 1, we saw that a galaxy's redshift increases when a galaxy is further away from us. Since light travels longer when it comes from a larger distance, light with a larger redshift is older. The spectrometer chip of DESHIMA uses this property by sorting light on frequency, and thus on redshift and age. The DESHIMA 2.0 chip has 347 logarithmically spaced bandpass filters, with center frequencies ranging from 220 to 440 GHz, see Figure 2.2. If a galaxy has a low redshift, z = 3.3 for example, its light has a high frequency and the 440 GHz filter gives a response; if a galaxy has a large redshift like z = 7.6, it has a lower frequency and the 220 GHz filter gives a response. After the light is sorted, it enters the Microwave Kinetic Inductance Detectors (MKIDs), where it is detected. Microwave Kinetic Inductance Detectors are incoherent detectors, meaning that they only measure the intensity of the signal and not the phase, and are hence not subject to quantum noise. A readout signal reads out the detected light using frequency division multiplexing. This has two advantages: the measuring bandwidth is decoupled from the readout bandwidth and the MKIDs can be read out simultaneously with a single pair of coax cables. The signal is read out with a frequency of 160 Hz. The spectrometer chip length is only a few centimeters as opposed to a meter in quasioptical instruments. Cooling multiple of these chips to 120 mK is feasible, making DESHIMA intrinsically scalable in bandwidth as well as number of pixels.

2.3. Microwave Kinetic Inductance Detectors

Microwave Kinetic Inductance Detectors (MKIDs) are radiation detectors that use a superconducting material. Superconductors have an energy gap of the order of a meV, which corresponds to a frequency of approximately

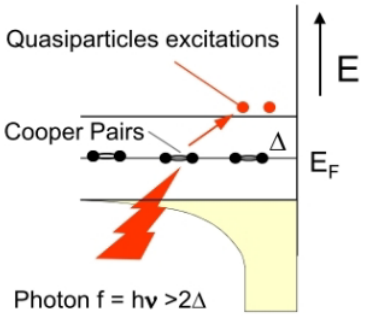

(a) Illustration of an incident photon breaking up a Cooper Pair into Quasiparticle excitations. The y-axis denotes the energy, where Δ is the gap energy of the superconducting material.

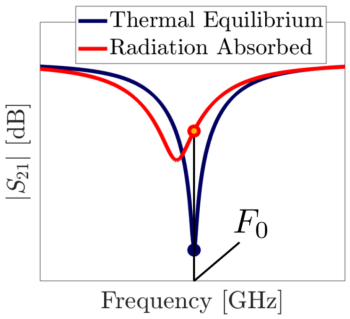

(b) Microwave transmission of a resonator versus frequency in the case of Thermal Equilibrium (blue) and when radiation is absorbed (red). F_0 denotes the resonant frequency when the material is in thermal equilibrium.

Figure 2.3: Both images are taken from [17].

100 GHz, which is perfect for our application. MKIDs are extremely sensitive and capable of making large detector arrays because of their limited frequency bandwidth. In addition, by cooling down the MKIDs to a temperature lower than approximately 1/10 of the critical temperature of the superconductor, thermal noise is suppressed very well. These properties make MKIDs extremely suitable for observations in the submillimeter domain.

Inside a superconductor, electrons are paired up in Cooper Pairs as this configuration is energetically favourable. When an incident photon has an energy of $E = hf > 2\Delta$, where h is Planck's constant, f is the frequency and Δ is the gap energy of the superconductor, it is able to break a Cooper pair into two quasiparticle excitations (see Figure 2.3a). Thus, when a higher number of photons is absorbed, the number of quasiparticles increases. As this increase affects the kinetic inductance, the resonant frequency of the resonator is lowered. Next to that, the quality factor is reduced as well. This can be seen in Figure 2.3b, where the peak becomes higher, broader and the peak value is shifted to the left when radiation is absorbed [17]. To read out the signal, the resonant frequency F_0 is constantly fed to the MKID, and its transmission is measured. When radiation is absorbed, the resonance frequency of the MKID decreases (see Figure 2.3b). This can be probed as a change in phase and amplitude of the microwave tone measured at the output of the readout microwave line.

2.4. De:code

De:code stands for DESHIMA code for Data Analysis and is the post-processing code of DESHIMA [18]. It is available as a python package and it extracts a galaxy spectrum from the data of DESHIMA. TiEMPO's output will be used as input for De:code, so that the features of De:code can be tested and improved.

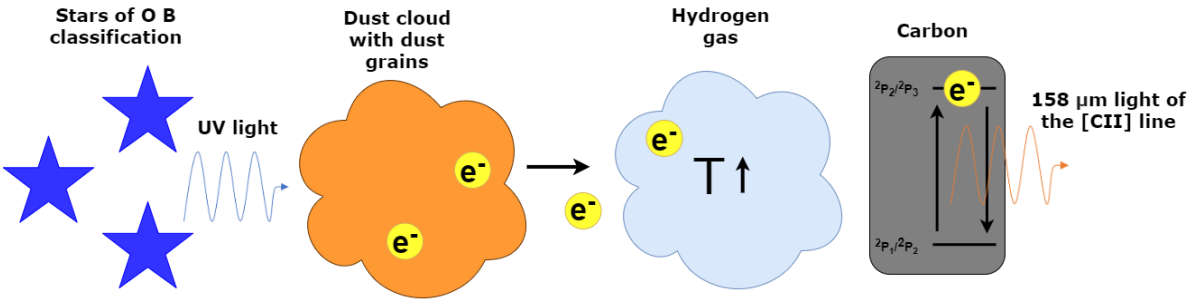

Figure 2.4: Illustration of the process causing the [CII] emission line. OB classified stars, which are typically heavy, hot and short-lived, emit ultraviolet light. This light causes electrons to be emitted by dust grains, via the photoelectric effect. These electrons heat up hydrogen gas. Hydrogen atoms collide with carbon atoms, exciting electrons and when these electrons fall back, the 158 μm (= $\frac{1.2\text{THz}}{c}$) light of the [CII] line is emitted [8]. This image is based on [21].

2.5. Emission lines

Carbon is ubiquitous in the Universe, making it very useful for galaxy research. The intensity of carbon emission lines in a galaxy gives a good estimate of its intensity of star formation, because carbon is naturally produced in stars [19]. Transitions in the energy shells (n shells) of an atom correspond to a large change of energy, resulting in photons in the optical or UV domain; fine structure transitions (transitions in the S and L subshells rather than the n shells) correspond to a smaller change of energy, resulting in mm/submm photons. Hence, we look at the fine structure line of singly ionized carbon (C^+), the so-called [CII] line.

Heavy, short-lived stars, which fall in the OB star classification, emit photons in the far UV domain, see Figure 2.4. These photons cause electrons to be emitted from dust grains in the dust cloud of a galaxy via the photoelectric effect. These electrons heat up hydrogen and helium gas, exciting carbon atoms by collisions. When the carbon atoms fall back to their original state, they emit photons in the fine structure line [20]. In this way, the intensity of [CII] line emission is related to the star formation rate in the galaxy.

The wavelength of the [CII] line, combined with the fact that it is the brightest emission line in an SMG makes it suited for our research. In addition to the [CII] line, we also look at the CO emission lines. Even though these are less bright, they consist of multiple linearly spaced lines, which enables us to determine the redshift unambiguously.

2.6. Observations of DESHIMA

The first light campaign of DESHIMA on ASTE in 2017 was very successful and provided a proof of concept for two applications of DESHIMA: as an efficient redshift machine and a multiline spectral mapper [2].

The first application was demonstrated by making a spectrum of VV 114, a luminous infrared galaxy, with only one bright emission line from CO, see Figure 2.5. The measured frequency of 339.0 GHz corresponds to the literature value of 345.796 GHz with a redshift of z = 0.02 [22]. This experiment shows that DESHIMA can be used to measure the redshift of SMGs and observe their emission line spectra.

The second application was demonstrated with a three-colour composite map of the Orion Nebula, consisting of maps of the CO(3-2), HCN(4-3) and HCO(4-3) emission lines, see Figure 2.6. This experiment was done using on-the-fly (OTF) mapping, meaning that the telescope observes while scanning across the sky. The coordinates of the telescope are accurately measured, making it possible to reconstruct an image from the OTF data [23]. The background radiation was removed by subtracting the signal common to all channels. This experiment demonstrates that DESHIMA can be used as a multiline spectral mapper using OTF mapping.

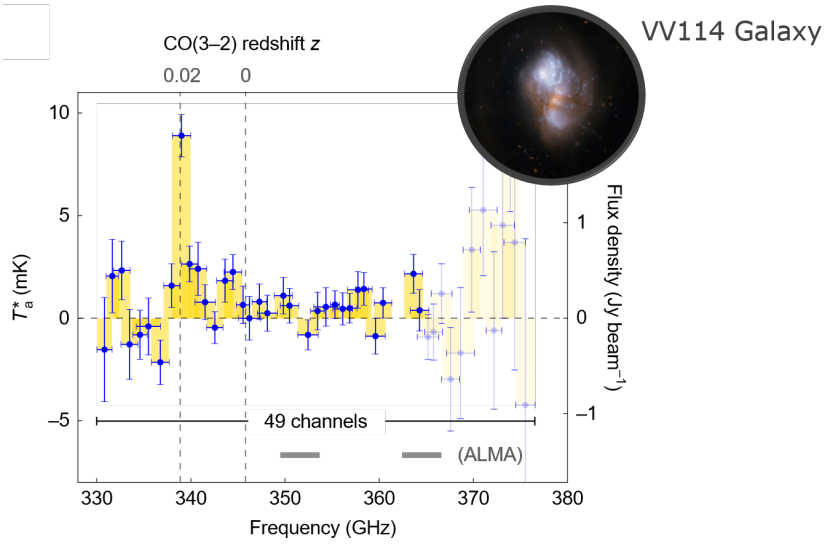

Figure 2.5: The spectrum of the VV 114 galaxy (a luminous infrared galaxy), made with DESHIMA. The CO(3–2) line is indicated in the graph. The horizontal dashed line represents the continuum flux for each filter in the DESHIMA chip. The yellow shading underneath the horizontal errorbars represents the full-width at half-maximum (FWHM) of the channel response, and the vertical errorbars stand for the standard deviation of the noise level per channel. The picture is taken from [2].

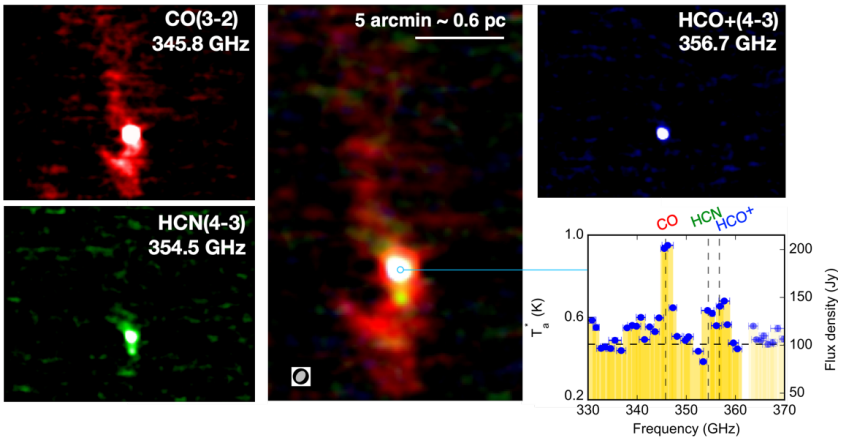

Figure 2.6: The image in the middle is an RGB image of the CO(3–2)/HCN(4–3)/HCO+ emission lines of the Orion Nebula, made with DESHIMA. The images on the left and on the top right show the maps of which the RGB image consists. The maps were produced by subtracting the continuum spectrum common to all filters in the spectrometer chip. The graph on the bottom right shows the spectrum of the Orion KL region, made with DESHIMA. The CO(3–2)/HCN(4–3)/HCO+ lines are indicated in the graph. The horizontal dashed line represents the continuum flux for each filter in the DESHIMA chip. The yellow shading underneath the horizontal errorbars represents the full-width at half-maximum (FWHM) of the channel response, and the vertical errorbars stand for the standard deviation of the noise level per channel. The picture is taken from [2].

2.7. DESHIMA 2.0

The improvements made in DESHIMA 2.0 are shown in Table 2.1. Most important to note, is that DESHIMA 2.0 is more efficient, more accurate, and more broadband with a bandwidth 5 times as large as in DESHIMA. DESHIMA 2.0 will be the first instrument to observe an octave bandwidth in the submillimeter domain.

Table 2.1: The improvements made in DESHIMA 2.0, compared with DESHIMA [2] [13].

Property	DESHIMA	DESHIMA 2.0
Misalignment DESHIMA and telescope	Not eliminated	Eliminated
Optical efficiency	2%	16%
Bandwidth (GHz)	332-337	220-440
Number of channels	49	347
Spectral resolution ($\frac{f}{\Delta f}$)	380	500

3

Model

3.1. Overview of the model

TiEMPO is an end-to-end model, containing models of SMGs, the atmosphere, the DESHIMA instrument and the spectrometer chip and its noise (see Figure 3.1). This chapter explains each of these components, elaborating on their properties and showing how TiEMPO models them.

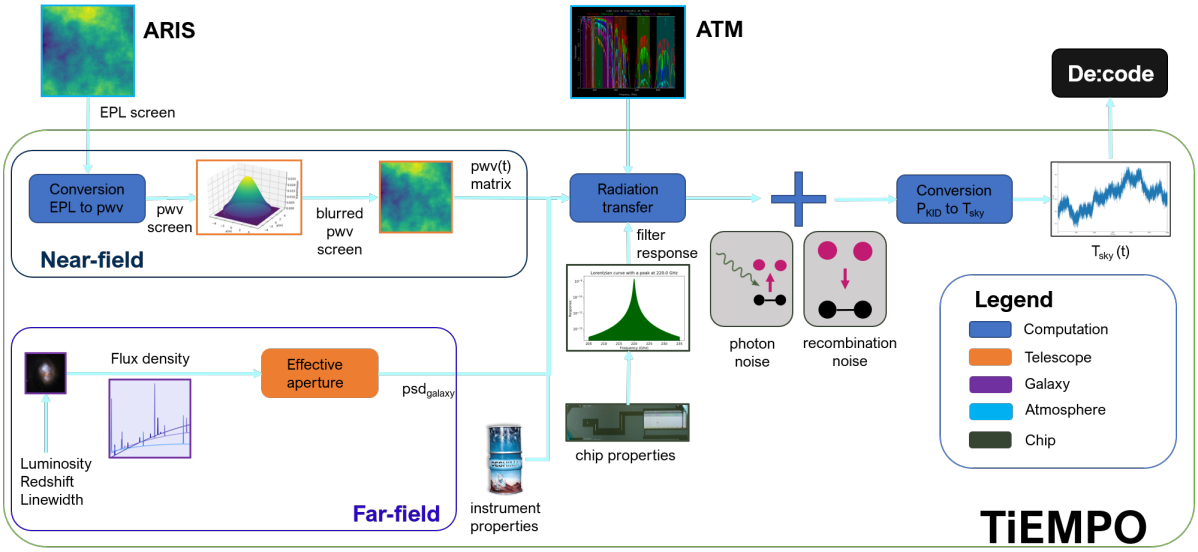

Figure 3.1: System decomposition of TiEMPO, showing each component with its input and output. The external models and algorithms that TiEMPO uses are shown as well. This Figure is meant as a reference and guide while reading this thesis.

3.2. Submillimeter-Bright Galaxies

Earlier, we saw that DESHIMA observes Submillimeter-Bright Galaxies, or SMGs, because these galaxies enable us to discover the history of the Universe. We can observe SMGs from the early Universe and they are the birthplace of many stars; in some SMGs, hundreds of solar masses of stars are formed per year [24]. However, they are hidden in thick dust clouds, making it hard to observe them. Dust particles absorb optical and ultraviolet emission from young stars, and re-radiate this light as infrared and submillimeter light, which is why we can observe SMGs with a submillimeter wave instrument, such as DESHIMA [25].

In our observations, we see two different kinds of emission: continuum and line emission. Continuum emission comes from interstellar dust and the Cosmic Microwave Background (microwave radiation originating from the Early Universe). This emission is thermal and can be described as blackbody radiation. Line emission comes from interstellar gas and is caused by atoms or molecules transitioning to another state, see Section 2.5.

In Section 2.5, we saw that the [CII] emission line is a good probe of a galaxy's star formation rate. In addition to that, CO emission lines can be used to measure a galaxy's redshift, because SMGs contain CO molecules in their reservoirs of molecular gas [26]. In addition, CO emission lines play a role in determining the star formation rate, defined as the mass of stars created in a galaxy in one year. The reason for this is that the star formation rate has a strong correlation with the column density of molecular hydrogen gas (H_2), see the Kennicutt-Schmidt law [27]. H_2 gas does not radiate in most cases but appears together with CO. Hence, we can use CO emission lines to estimate the column density of H_2 and ultimately, determine the star formation rate.

3.2.1. Implementation

The luminosity, redshift and linewidth are input parameters of the model. TiEMPO treats the galaxy as a point-source, which is justified, as the angular size of the galaxies of interest is approximately 10 times as small as the far-field beam of DESHIMA 2.0 [28]. The galaxy model inside TiEMPO simulates a galaxy using a two-component modified blackbody spectrum as a template [29].

The galaxy model simulates the continuum emission with Planck's law, which gives the spectral radiance of a blackbody for a given frequency f and temperature T:

$$B_f(f,T) = \frac{2hf^3}{c^2}\frac{1}{e^{\frac{hf}{k_B T}} - 1}, \tag{3.1}$$

where B_f is the spectral radiance in W sr^{-1} m^{-2} Hz^{-1}, f the frequency, ant T the temperature. Because of the redshift, the observed frequency is not equal to the emitted frequency, so we first need to determine the rest frequency with

$$f_{rest} = f_{obs}(1+z), \tag{3.2}$$

where f_{rest} is the rest frequency of the galaxy, and f_{obs} is the observed frequency.

The emission lines are simulated with Gaussian peaks around their center frequency. From the input luminosity, the line luminosity is calculated for each spectral line in the model, using the line flux ratios from [30] and [31]. Then the flux amplitude of each line is computed using the input linewidth (or velocity width), so that the integral of the flux density of the spectral line equals its flux (the astronomical distance in the model is determined using [32]).

In the graph below, we show an example of a galaxy spectrum generated by the model. The galaxy model outputs the flux density in Jansky. TiEMPO then calculates the effective aperture area and multiplies this with the flux density in order to obtain the power spectral density of the galaxy. This psd is later added to the psd of the cosmic microwave background when the telescope is pointing at the galaxy (on-source). When it is not pointing at the galaxy (off-source), only the psd of the cosmic microwave background is used.

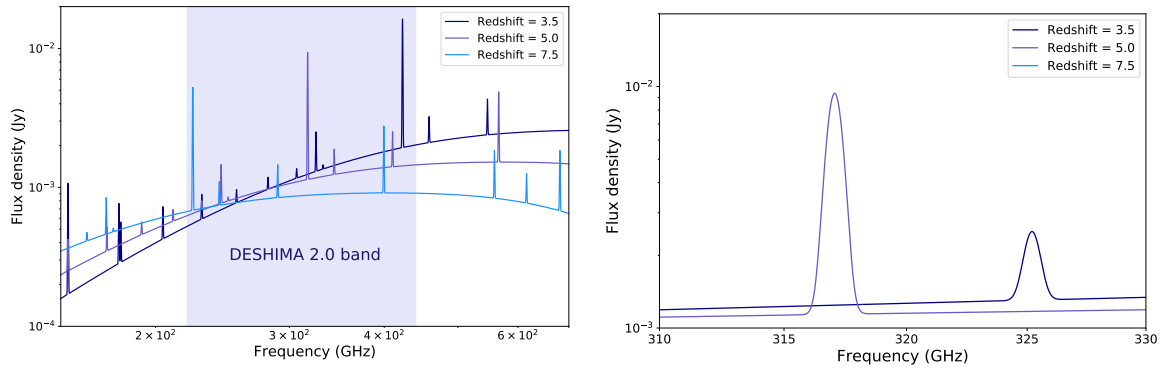

(a) The complete spectrum.

(b) Zoom-in on emission lines, showing the Gaussian peak shape.

Figure 3.2: The spectral energy distribution of a typical submillimeter-bright galaxy, generated by the model of Tom Bakx (private communications). The graph shows the flux density in Jansky plotted against the frequency in GHz for different values of the redshift.

3.3. ATMOSPHERE

Millimeter-submillimeter waves passing through Earth's atmosphere are partly absorbed and re-radiated by water vapor. Before this project, the effect of the atmosphere on the signal had only be simulated statically, using desim [33]. In TiEMPO, we require a dynamic model of the atmosphere. In order to do this, we need time domain data of the water vapor in the Atacama Desert. The amount of water vapor can be expressed using the precipitable water vapor, or pwv, which denotes the height of the water column obtained if all water vapor were precipitated as rain. As time-dependent data of the pwv are unavailable, we used Extra Path Length data and converted this to pwv data. Waves that pass through the atmosphere obtain an Extra Path Length, meaning that their optical path length fluctuates [34]. This excess path can be expressed by the spatial structure function, which represents the mean-square difference between the fluctuations at two different positions, separated by displacement vector s [35].

$$D(s) = \langle [\Phi(x+s) - \Phi(x)]^2 \rangle, \tag{3.3}$$

where Φ is the fluctuation in EPL and x is the position. To use this, the Astronomical Radio Interferometer Simulator (ARIS) is used [1] [36]. ARIS approximates the spatial structure function as

$$\begin{aligned} D(s) &= C^2 s^{\frac{5}{3}} && (s \leq L_1), \\ D(s) &= C^2 L_1 s^{\frac{2}{3}} && (L_1 < s \leq L_2), \\ D(s) &= C^2 L_1 L_2^{\frac{2}{3}} && (s > L_2), \end{aligned} \tag{3.4}$$

where L_1 and L_2 denote the inner and outer scales, i.e. the minimal and maximal correlation length for water vapor fluctuations in the troposphere (the lowest layer of the atmosphere on Earth). C is a structure coefficient. These equations assume that the structure of phase fluctuations is invariant when the atmosphere moves with the wind. Even though this is an idealization, it has been confirmed for observations up to 1 km by Gurvich et al [37]. Furthermore, only Kolmogorov turbulence (statistically isotropic turbulence [38]) is taken into account and the fluctuations are modeled as a two-dimensional phase screen at 1 km altitude. This altitude is close to the average exponential scaleheight - the height at which the pwv value has dropped below $1/e$ times the median value - which equals 1.13 km [39]. Furthermore, the root-mean-square deviation of the EPL is an input parameter in ARIS.

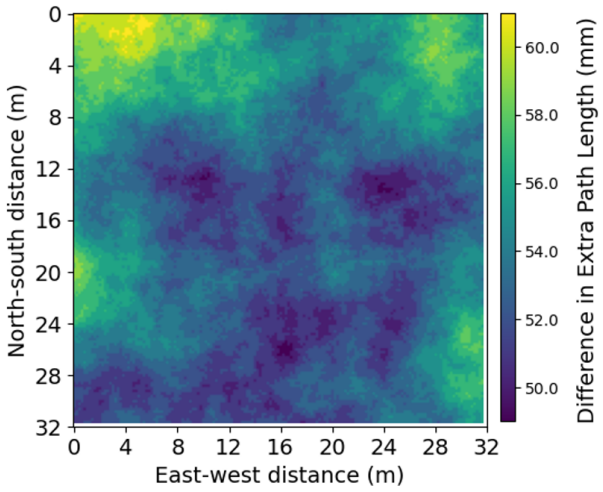

Figure 3.3: A colormap of the output of ARIS for a 32 x 32 m sky window.

In the simulations done in this thesis, this RMS was taken to be 50 μm. Figure 3.4 shows the pwv plotted against time for different timescales (1 minute, 60 minutes, and 5 hours). The shaded area denotes the area in which the pwv is within one standard deviation of the average value. We observe that the atmosphere fluctuations are smaller than a standard deviation on a small timescale, and increase with an increasing timescale. By using ARIS, TiEMPO assumes that atmosphere noise is caused exclusively by water vapor. It was found by Sewnarain Sukul, Y., that the fluctuations in the sky temperature were mainly caused by fluctuations in the precipitable water vapor during DESHIMA observations [14], justifying this assumption.

ARIS outputs a two-dimensional map of the fluctuations in Extra Path Length (dEPL) on a sky window. Figure 3.3 shows the output of ARIS on a 32 x 32 m window. In order to fulfill the requirements of TiEMPO, a large improvement on ARIS was made (Yoshiharu Asaki, private communications and [40]). First of all, as TiEMPO will execute simulations of 8-hour observations, ARIS must be capable of making very long atmosphere screens. In the DESHIMA data that was used for validating TiEMPO, the windspeed was 0 m/s to 16 m/s. For an 8-hour observation, this results in an atmosphere screen with a length of up to to 460.8 km, which is an enormous increase from the 1 km screen that ARIS was first capable of creating.

For the width of the atmosphere screen, sky chopping and nodding of DESHIMA 2.0 determine the requirement. Sky chopping and nodding are movements of the telescope (instrument), that enable the removal of the atmosphere noise from the signal (see Section 3.4.3 for a more rigorous explanation). The radius of the telescope beam, combined with the chopping separation of approximately 1.13 m, gives a minimal required width of $2 \cdot 10 + 1.13 = 21.13$ m. To prevent influences from boundary effects on our signal, we took a screen width of 25 m.

Finally, the grid resolution requirement is determined by the need to resolve the difference between two chop positions. The grid resolution must be smaller than the chopping separation of 1.13 m. The observations in this thesis have been made with a grid resolution of 0.2 m.

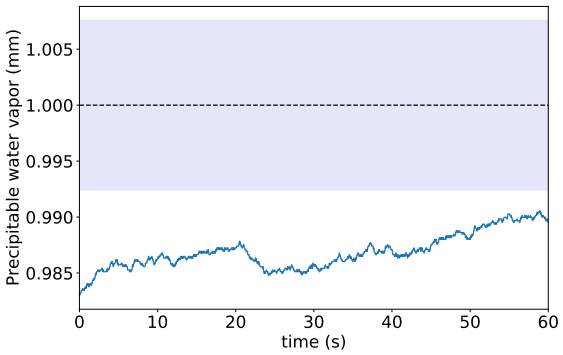

(a) One minute time interval

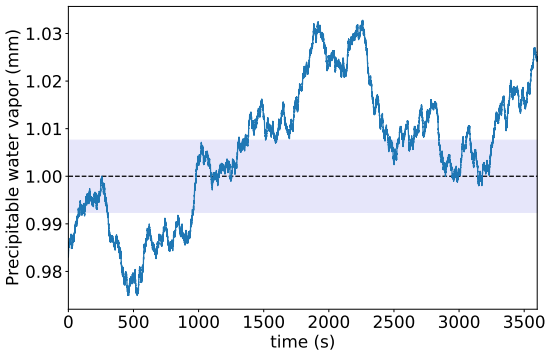

(b) 60 minute time interval

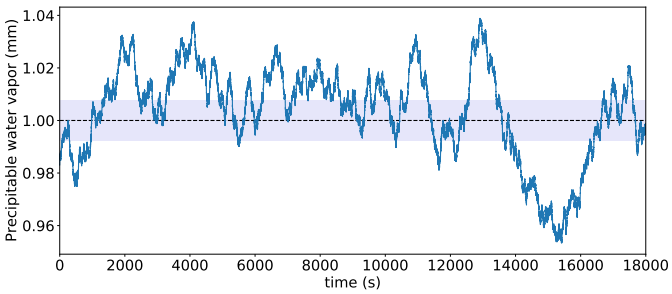

(c) 5 hours time interval

Figure 3.4: The precipitable water vapor (pwv) in mm plotted against the time in seconds. In this atmosphere simulation, an average pwv of 1.0 mm was used, denoted by the dashed line. The shaded area denotes the area in which the pwv is within one standard deviation of the average value.

3.3.1. Conversion from EPL to pwv

Since we are using the pwv value in the rest of the model, we need to find a relation between the difference in precipitable water vapor and the difference in Extra Path Length.

The relation is of the kind

$$\mathrm{dpwv} = \frac{1}{a}\mathrm{dEPL}, \tag{1}$$

where dpwv and dEPL are both in m. In order to find a, we will use the Smith-Weintraub value of the extra path length [41], [42], which is given below.

$$\mathrm{EPL} = \frac{h}{10^6}(k_2\frac{e}{T} + k_3\frac{e}{T^2}), \tag{3.5}$$

where $k_2 = 70.4 \pm 2.2$ K/mbar and $k_3 = (3.739 \pm 0.012) \cdot 10^5$ K^2/mbar [43] [42]. h is the height of the column of air in m, T the temperature of the column in K and e is the partial pressure of water vapor in mbar. The first term represents distortions of electronic charges of dry gas molecules as a result of an electromagnetic field; the second term represents the effect, that the orientation of the electric dipoles of water vapor have when an electromagnetic field is applied.

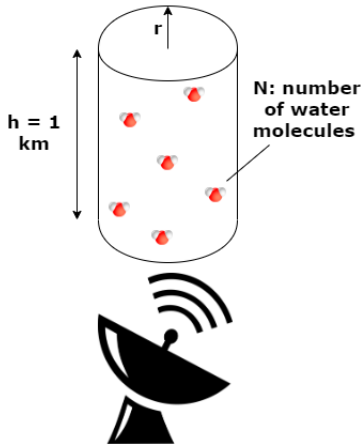

Figure 3.5: Illustration of the cylinder of air above the telescope, that is used in the derivation of a relationship between EPL and pwv.

We will find an expression for e using the ideal gas law. The ideal gas law is given by

$$e\,V = N R\,T, \tag{3.6}$$

where V is the volume in m^3, N is the number of water molecules and R is the gas constant and has a value of $R = 8.314$ J/mol·K [44].

We consider a cylinder of air, which we model with a cylinder containing water vapor. As the largest contribution to noise from the atmosphere comes from water vapor, other gases have not been taken into account in the model, see Figure 3.5. The volume of this cylinder can be expressed as

$$V = h\,\pi\,r^2, \tag{3.7}$$

whereas the number of water molecules is given by

$$N = pwv\,\pi\,r^2\,\rho, \tag{3.8}$$

where ρ is the number density of water molecules in m^{-3}. Hence, combining equation (3.6), (3.7) and (3.8), we obtain the following expression for e.

$$e = \frac{1}{h}\,\rho\,R\,\mathrm{pwv}\,T. \tag{3.9}$$

Combining this result with equation (3.5), we obtain

$$\mathrm{EPL} = 10^{-6}\rho R(k_2 + \frac{k_3}{T})\,\mathrm{pwv}. \tag{3.10}$$

When we take the absolute temperature to be $T = 275$ K, $\rho = 55.4 \cdot 10^3$ mol/m^3 and $R = 8.314 \cdot 10^{-2}$ mbar m^3/K· mol, we obtain $a = 6.587$. This value is used to convert the dEPL map into a dpwv map, see Figure 3.6 or [1] for an animation of the moving atmosphere.

[1] https://www.youtube.com/watch?v=YoI3vVl-ZiU

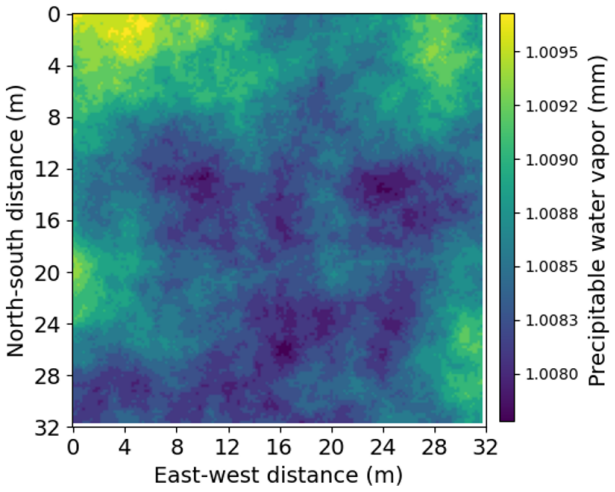

Figure 3.6: A colormap of the output of ARIS for a 32 x 32 m sky window converted to pwv with Equation (3.10).

3.3.2. Implementation

ARIS outputs a grid of dEPL values. TiEMPO converts this to dpwv values and stores these values in an array. To go from dpwv to pwv, TiEMPO adds a slowly-varying or constant average pwv value to dpwv:

$$\mathrm{pwv} = \mathrm{dpwv} + \mathrm{pwv}_0, \tag{3.11}$$

where pwv_0 has been taken around 1-2 mm in this thesis, because this is characteristic for the Chajnantor Plateau, where the telescope is located, as Figure 3.7 shows. In the simulations where we compared the model output with DESHIMA observations, we took the pwv measured at the start of the observation as pwv_0.

After this array is modified by the telescope model (see the section below), TiEMPO uses it as a lookup table - it connects a moment in time and a value for the windspeed to a position in the array and uses this value as pwv. This pwv value is converted to atmospheric transmission in desim, by means of an interpolation function made of an atmospheric transmission table [33]. The data in this table were obtained using the ATM model [15], [16].

3.4. Observing with the telescope

3.4.1. Near-field beam

We approximated the beam of radiation of the ASTE telescope with a Gaussian beam for simplicity and because a Gaussian shape is similar to the real beam shape of the ASTE telescope. The beam is focused into the telescope cabin of ASTE with a primary and a secondary mirror. The secondary mirror has a spillover to the sky with a much larger solid angle than the primary beam, which is not yet modeled in TiEMPO. If a higher precision is required, however, TiEMPO can use any arbitrary beam shape, also including the spillover.

As the Fourier transform of a Gaussian function is a Gaussian function again, the aperture plane illumination also has this shape [46]. The Gaussian curve that we use in the model is truncated at the edge of the primary mirror and its the total volume equals 1. We take the peak of our truncated Gaussian function to be at (0, 0) coordinates. The Gaussian function is symmetric in the x-axis and y-axis, as the aperture is circular. We have $\sigma_X = \sigma_Y = \sigma$ and obtain the following expression:

$$f(x, y) = Ae^{-(\frac{x^2}{2b^2} + \frac{y^2}{2b^2})}. \tag{3.12}$$

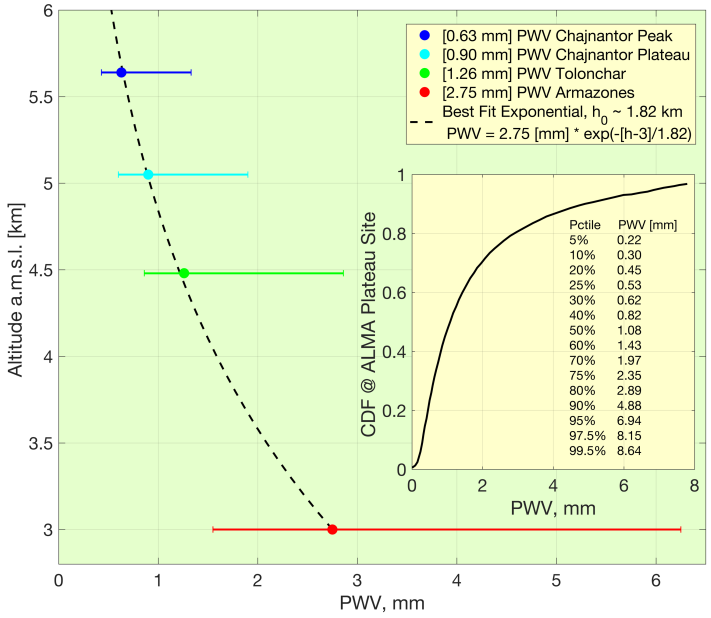

Figure 3.7: The altitude in km versus the pwv in mm. The light blue point is measured at the Chajnantor Plateau, where ASTE is located. The error bars indicate the 25 and 75 percentile levels. This figure is taken from [45].

The radius at the truncated edge of the telescope beam is 5 m and the height of the surface at the sides is approximately 10 % of its maximal height (Nuria Llombart, private communications). We determine the b parameter as follows

$$\begin{aligned} f(x^2+y^2=25) &= \frac{1}{10}A \\ Ae^{-\frac{25}{2b^2}} &= \frac{1}{10}A \\ b &= \sqrt{\frac{25}{2ln(10)}} \approx 2.33. \end{aligned} \tag{3.13}$$

For the total volume of the Gaussian to equal 1, we must have

$$\begin{aligned} V &= 2\pi Ab^2 = 1 \\ A &= \frac{1}{2\pi b^2} \approx 0.029. \end{aligned} \tag{3.14}$$

With this, the expression for the Gaussian is completely determined and has the shape shown in Figure 3.8.

The atmosphere data from the model, consisting of pwv values (see Section 3.3), was filtered with this Gaussian function to simulate the telescope beam, as shown in Figure 3.9.

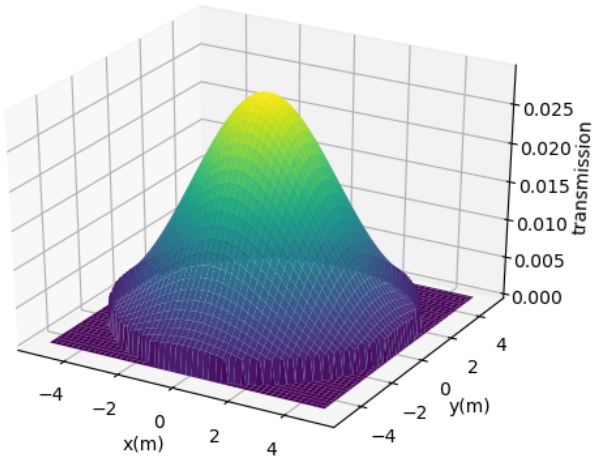

Figure 3.8: The truncated Gaussian that is used as telescope beam shape in the model. The total volume of the Gaussian equals 1 and it is truncated at a radius of 5 m, where its height is 10 % from its peak height.

3.4.2. Far-field beam

The far-field telescope beam is characterized by two properties: the main beam solid angle and the main beam efficiency. The main beam solid angle Ω_{MB} in sr denotes the solid angle of the beam without the side-lobes. The main beam efficiency η_{MB} tells us the fraction of the beam contained in the main beam. The beam solid angle, with the side-lobes included, is then given by

$$\Omega_A = \frac{\Omega_{MB}}{\eta_{MB}}. \tag{3.15}$$

We use the beam solid angle to determine the effective aperture area in m^2:

$$A_e = \frac{\lambda^2}{\Omega_A}. \tag{3.16}$$

Now, we can express the antenna efficiency η_A, expressing the fraction of the geometrical aperture A_p that is contained in the effective aperture area

$$\eta_A = \frac{A_e}{A_p} = \frac{\eta_{MB}}{\Omega_{MB}} \frac{\lambda^2}{A_p}. \tag{3.17}$$

The effective aperture area is used to obtain a power spectral density of the galaxy flux density provided by the galaxy component. This power spectral density is calculated as follows

$$psd_{galaxy} = \frac{1}{2} F_f A_e, \tag{3.18}$$

where F_f denotes the flux density in Jy and the factor $\frac{1}{2}$ compensates for the fact that the flux density is calculated using two polarizations, but the power spectral density is single-polarization.

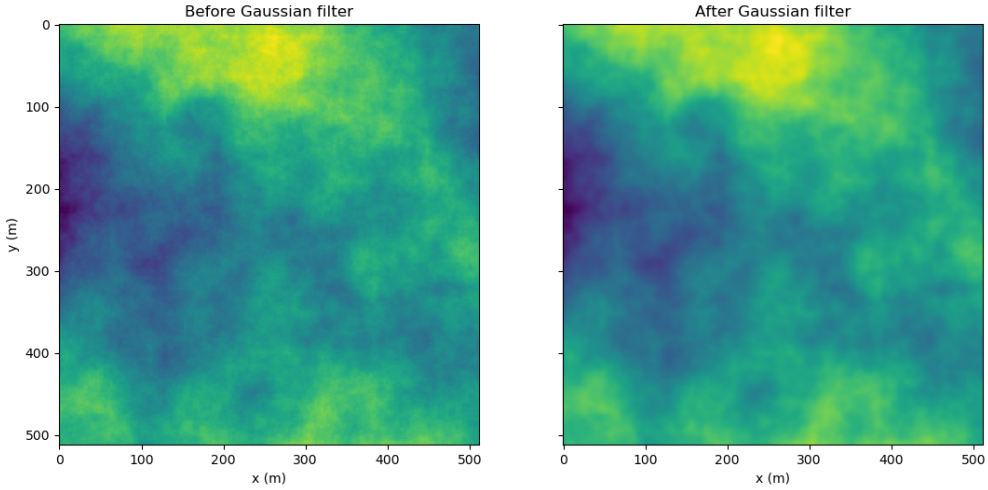

Figure 3.9: An atmosphere window of 500 by 500 m before and after applying a Gaussian filter.

3.4.3. Sky chopping

A telescope receives radiation from both the atmosphere and the galaxy or other heavenly body behind the atmosphere. For astronomical research, only the latter one is of interest, so we need to remove the radiation of the atmosphere from our signal. In order to do this, we use sky chopping and nodding, which will both be explained in this section.

Sky chopping means rapidly switching between two positions on the sky using a chopper wheel, shown in Figure 3.10. It is an improvement made in DESHIMA 2.0, and was not possible yet with the DESHIMA instrument. The chopping wheel is made of reflecting material and has 2 incisions. If the signal comes in while there is no incision at the point where both channels come together, it is reflected and the light from position 1 is measured. If the signal comes in while one of the incisions is at the point where both channels come together, the light from position 2 is measured. Choosing the right distance between the two chop positions is crucial: choose them too close to each other and the source will be observed in both positions; choose them too far apart and the atmosphere will be significantly different in both positions, making it more difficult to properly remove the atmosphere radiation from the signal. In our case, the optimal separation is 100.5 mm, which corresponds to a separation of 233.6 arcseconds on sky (calculated with a phase screen at 1 km height).

Sky chopping is effective in removing the atmosphere signal while retaining the galaxy signal, because of the difference between the near and the far field (see Figure 3.11). In the near field, the different beams are almost parallel and do not diverge yet. This causes the beams to overlap almost entirely, so that the atmosphere signal in both beams is almost identical. In the far field, the beams have diverged and now have a separation of 233.6 arcseconds in the case of the ASTE telescope. The beam size is now 16 to 32 arcseconds (the far-field beam is frequency-dependent: the larger the frequency, the sharper the far-field beam), meaning that a galaxy lies entirely inside the beam. Hence, the beam of the ON position receives the galaxy signal, whereas the beam of the OFF position does not.

Sky nodding means moving the telescope dish to another point. The method that is most commonly used in astronomy is the ABBA method. In this method, chopping and nodding are alternated to optimally subtract the atmosphere signal. There are three different sky positions, called sky A, sky B and sky C, see Figure 3.12. The source is at sky position B. Furthermore, there are two nod positions, nod A and nod B and within both nod positions, we have chop b and chop a, with chop a being the right position and chop b being the left. Suppose we start at time t_1 in nod position a and chop the telescope between chop a and chop b. We measure the following radiation

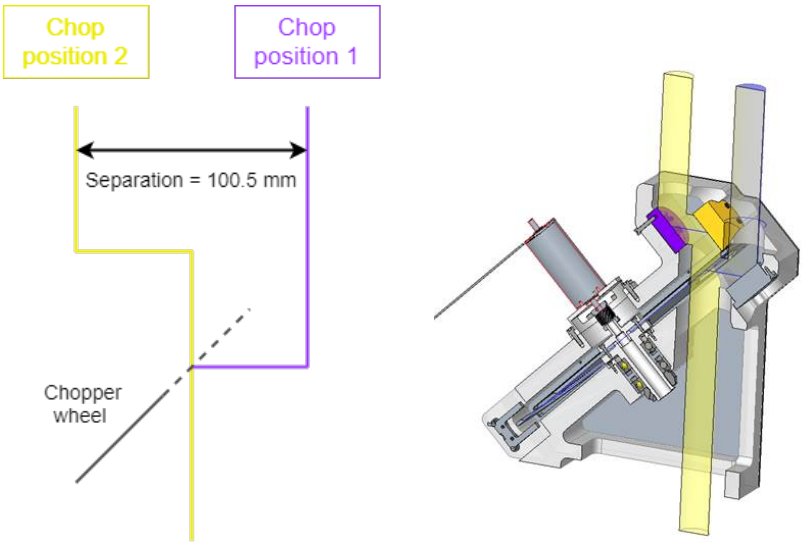

(a) Illustration of the working of the chopper wheel

(b) 3D drawing of the chopping instrument

Figure 3.10: Drawings of the chopping instrument. The chopping wheel is made of reflecting material and has 2 incisions. If the signal comes in while there is no incision at the point where both channels come together, it is reflected and the light from position 1 is measured. If the signal comes in while one of the incisions is at the point where both channels come together, the light from position 2 is measured. These pictures are from Robert Huiting and Stephen Yates (private communications).

$$\begin{array}{ll} \text{nod A, chop A:} & skyB_1 + source \\ \text{nod A, chop B:} & skyA_1, \end{array} \tag{3.19}$$

where the subscript denotes the point in time [47]. If we then move the telescope to nod B and chop again, we measure at time t_2

$$\begin{array}{ll} \text{nod B, chop A:} & skyC_2 \\ \text{nod B, chop B:} & skyB_2 + source. \end{array} \tag{3.20}$$

Finally, another observation is done in this position and afterwards the telescope is moved back again to nod A where the last observation is done. This gives

$$\begin{array}{ll} \text{nod B, chop A:} & skyC_3 \\ \text{nod B, chop B:} & skyB_3 + source \\ \text{nod A, chop A:} & skyB_4 + source \\ \text{nod A, chop B:} & skyA_4. \end{array} \tag{3.21}$$

The order of the nod positions is now spelled ABBA, explaining the name of the method. Determining the differences between these positions gives:

$$\begin{array}{ll} t_1: & \text{chop A - chop B} = skyB_1 - skyA_1 + source \\ t_2: & \text{-(chop A - chop B)} = skyB_2 - skyC_2 + source \\ t_3: & \text{-(chop A - chop B)} = skyB_3 - skyC_3 + source \\ t_4: & \text{chop A - chop B} = skyB_4 - skyA_4 + source. \end{array} \tag{3.22}$$

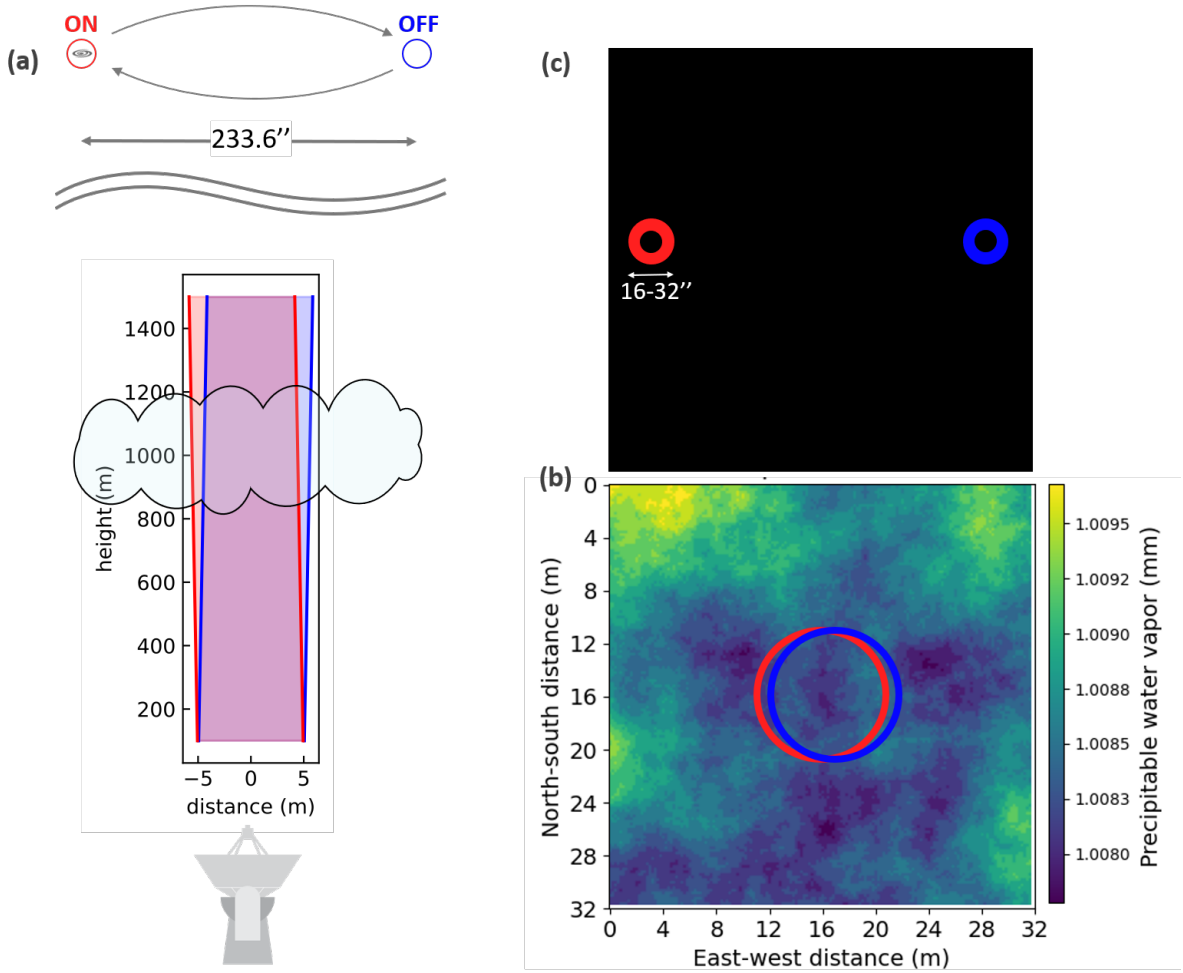

Figure 3.11: **a. Illustration of the ON and OFF position during skychopping**. When we observe the near-field beam, we see that there is much overlap between the ON and OFF beams (see the shaded areas in red and blue). In the far-field beam, the positions are completely separated and the size of the beam is so large, that the galaxy is seen as point-source (the galaxy is completely within the beam in the ON position). **b. Beam separation in the near field**. The beam separation is shown on scale on the atmosphere phase screen. **c. Beam separation in the far field**. The beam separation is shown on scale on the atmosphere screen. The beam size is 16 to 32 arcseconds (the larger the frequency, the smaller the far-field beam size).

Averaging this difference yields

$$\overline{\Delta} = \frac{skyB_1 + skyB_2 + skyB_3 + skyB_4}{4} - \frac{skyA_1 + skyC_2 + skyC_3 + skyA_4}{4} + source. \tag{3.23}$$

Assuming that the changes in atmosphere are gradual, we obtain linear gradients across the sky, yielding

$$skyA_{i+1} = skyA_i + a\Delta t_{i+1\to i} \tag{3.24}$$

for time i and position A, where a is the gradient and $\Delta t_{2\to 1} = t_2 - t_1$. Equations with sky positions B and C are equivalent, with gradients b and c, respectively. If we assume that the spatial structure of the sky is linear in the horizontal direction as well, we obtain

$$skyB_i = \frac{skyA_i + skyC_i}{2} \tag{3.25}$$

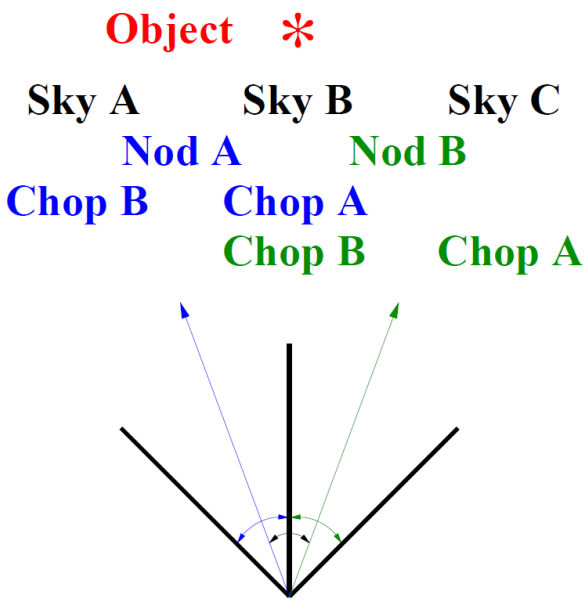

Figure 3.12: Illustration of the different chopping and nodding positions, taken from [47]. There are 3 sky positions, A, B, and C. The source (Object) is at sky position B. Depending on the position of the nodding, the telescope can have chopping position A or B, which is shown with blue and green.

for each time i, and $b = (a + c)/2$. Now we obtain an averaged difference of

$$\begin{aligned}\overline{\Delta} &= \frac{b(\Delta t + 2\Delta t + 3\Delta t)}{4} - \frac{a(3\Delta t)}{4} - \frac{c(\Delta t + 2\Delta t}{4} + source \\ &= \frac{(a+c)/2(\Delta t + 2\Delta t + 3\Delta t)}{4} - \frac{a(3\Delta t)}{4} - \frac{c(\Delta t + 2\Delta t)}{4} + source \\ &= source.\end{aligned} \tag{3.26}$$

We see that the ABBA method cancels out the influence of the atmosphere very well and this method is hence preferred over other methods.

3.4.4. Implementation

In each time iteration, TiEMPO computes the resulting signal for five different values of the pwv. Figure 3.13 shows these five positions relative to each other. The object to be observed is at the position in the center. This shape enables sky-chopping with the ABBA method (described in the previous section), both parallel and perpendicular to the wind direction (the wind direction is the horizontal direction in the picture).

3.5. DESHIMA simulator (desim)

For the DESHIMA instrument part of the model, a subset of the DESHIMA simulator - desim - was used [33]. Each component is modelled as a blackbody. The power spectral density of Johnson-Nyquist noise is given by

$$psd = \frac{hf}{e^{\frac{hf}{k_B T}} - 1}, \tag{3.27}$$

where h is Planck's constant, f the frequency, k_B is Boltzmann's constant and T is the temperature [48]. desim calculates the power spectral density of each medium in the DESHIMA instrument using Expression (3.27). The final power spectral density is then computed by cascading the radiation transfer of each component of DESHIMA: the cryostat window, the mirrors, the quasioptical filters, and the lens-antenna (see Section 2.1).

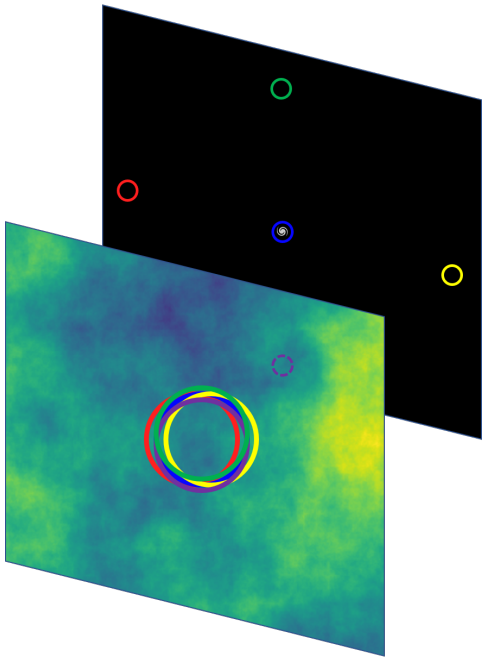

Figure 3.13: The positions of the pwv values are taken in the DESHIMA model for each time iteration. In the near field, the beams of the different positions almost completely overlap, whereas the beams are fully separated in the far field. The galaxy is located in the center position.

The radiation transfer equation is given by

$$psd_{out} = \eta\, psd_{in} + (1-\eta) psd_{medium}, \tag{3.28}$$

where psd_{out} is the psd of the radiation that comes out of the component, psd_{in} the psd of the radiation going in, η the transmission of the medium (the fraction of the power that is transmitted) and psd_{medium} is the power spectral density of the medium. In the first (blue) term, part of the radiation is absorbed by the component; in the second (orange) term, radiation is emitted by the component (Figure 3.14 shows this for η_{atm}, where the atmosphere attenuates the astronomical signal (blue), and emits radiation (orange).

3.6. MKID chip

3.6.1. Filter response

We approximated the filter response curve of each channel in the MKID chip with a Lorentzian curve. A comparison between the predicted filter response and the Lorentzian curve is shown in Figure 3.15. TiEMPO works with any arbitrary filter response curve, so measured and simulated filter responses can be incorporated in TiEMPO. We have used a Lorentzian curve as a filter response shape. This was implemented by dividing the complete frequency range of 220-440 GHz into 1500 bins, see Figure 3.16. For each of these bins, the value of the Lorentzian curve corresponding to the filter in question is calculated and is multiplied by the efficiency of the chip, η_{chip}. The resulting efficiency is used to compute the power spectral density with the radiation transfer equation that we saw in Section 3.5. Finally, the power in a bin is calculated using

$$P_{bin} = \Delta f\, psd_{bin\, i}. \tag{3.29}$$

The power of all bins is added together to obtain the total power P_{MKID}, after we have added noise (see Subsection 3.6.2).

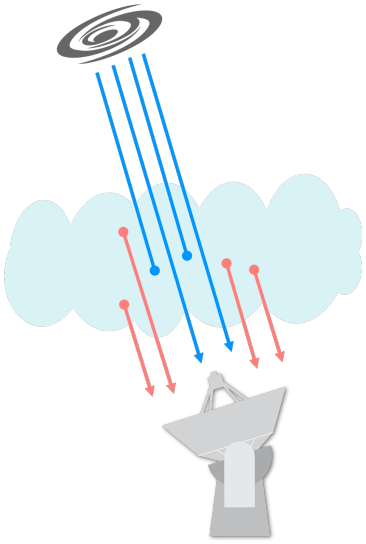

Figure 3.14: Illustration of absorption and emission by the atmosphere. The blue term in Equation (3.28) denotes the absorption and the orange term the emission.

3.6.2. NOISE AND NEP

In addition to the atmospheric noise, there are three kinds of noise we took into account: Poisson noise, photon bunching and recombination noise. Poisson and photon bunching noise together form photon noise, which, even though it is independent of the atmospheric transmission, originates mainly from the atmosphere. Poisson noise is caused by the random arrival time of photons. Photon bunching occurs when a stream of photons is observed. Even though the atoms inside the source (the galaxy, for example) emit waves completely independently from each other, these waves interfere with one another, causing the photons to arrive in 'bunches'. Photon bunching increases noise and this has to be taken into account in the modeling of the MKID. Finally, recombination noise occurs in a superconductor, as quasiparticle excitations recombine into Cooper pairs with a random lifetime. In addition, there can be low-frequency excess noise because of fluctuations caused by the two-level system in the dielectrics of the MKIDs. This noise is not included in TiEMPO [2].

These three sources of noise are modeled using the noise equivalent power, or NEP. The NEP of a signal is defined as the signal power that gives a signal-to-noise ratio of 1 for an integration time of 0.5 seconds [50]. The expression for the NEP is given by

$$NEP_{ph} = \sqrt{2P_{KID}\Big(\underbrace{hf}_{\text{Poisson noise}} + \underbrace{\frac{P_{KID}}{\Delta f}}_{\text{photon bunching}}\Big) + \underbrace{4\Delta_{Al}\frac{P_{KID}}{\eta_{pb}}}_{\text{recombination}}}, \tag{3.30}$$

where P_{MKID} is the KID power of the frequency bin in question, Δf is the effective bandwidth of the frequency bin, Δ_{Al} is the superconducting gap energy of aluminium, equal to $\Delta_{Al} = 188\ \mu\text{eV}$ and η_{pb} is the pair-breaking efficiency, given by $\eta_{pb} \approx 0.4$ [2].

[2] Kaushal Marthi is working on an implementation of this noise.

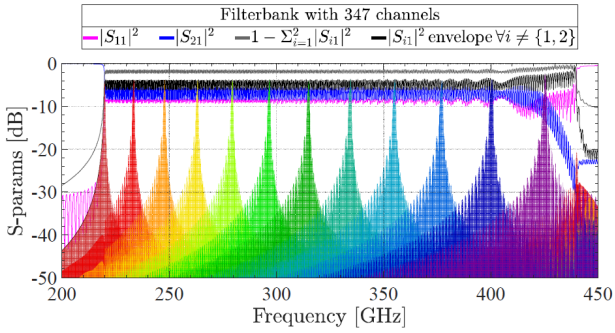

(a) The predicted filter response curves of the channels of DESHIMA 2.0. [49].

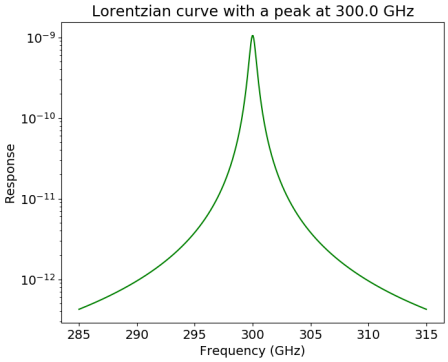

(b) Plot of a Lorentzian curve, centered at 300 GHz. This curve was used in the model to approximate the filter response and is normalized so that its integral equals 1.

Figure 3.15: The predicted filter response and the estimation of the filter response used in the model.

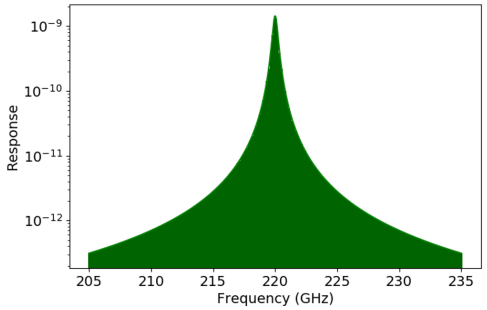

(a) The filter with the lowest center frequency, 220 GHz, with the bins used in the model.

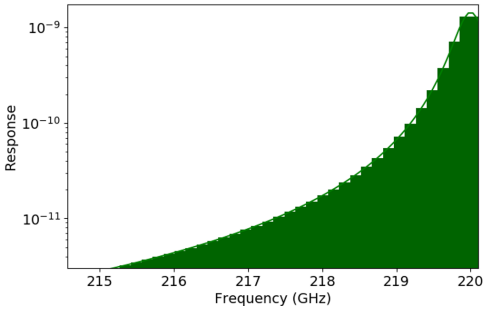

(b) The filter with the lowest center frequency, 220 GHz, with the bins used in the model, zoomed in.

Figure 3.16: The bins used in the model are shown on the least well sampled filter. These Figures show that the filter response is very well approximated by the bins.

Photons are bosons, meaning that, unlike fermions, an arbitrary number of them can occupy the exact same energy state. Bosons can be described by Boltzmann statistics and hence the number of photons absorbed per coherence time $t_{coh} = \frac{1}{\Delta f}$ is

$$n(f, T_{load}) = \frac{1}{e^{\frac{hf}{kT_{load}}} - 1}. \tag{3.31}$$

If the detector is coupled directly to a blackbody with a temperature T_{load}, this number can also be determined from the power as follows:

$$n = \frac{P_{MKID}}{\Delta f h f}. \tag{3.32}$$

The photon bunching term in equation (3.30) is based on this expression.

3.6.3. Poisson distribution

In the limit of n « 1 per coherence time, we can treat the detection of photons as independent events happening randomly. We can thus apply Poisson statistics to this situation and use the Poisson distribution to simulate noise. The Poisson distribution is given by

$$\mathbb{P}(n) = \frac{\overline{n}^n}{n!} e^{-\overline{n}}, \tag{3.33}$$

where n is the number of photons per coherence time [51]. Generation-recombination noise can be described by a Poisson distribution as well. Quasiparticle excitations recombine with a random lifetime, causing Poisson distributed noise.

3.6.4. LIMIT OF THE POISSON DISTRIBUTION

In this section we show that the Poisson distribution approaches a Gaussian distribution when n goes to infinity. We take the Poisson distribution, $\mathbb{P}(n) = \frac{\overline{n}^n}{n!} e^{-\overline{n}}$, with $\overline{n} = \mathbb{E}(n) = \lambda$ and let $n = \lambda(1+\delta)$, where $\lambda \gg 1$ and $\delta \ll 1$. This is justified as we are looking at the limit of $n \to \infty$. We use Stirling's formula [52], which is given by

$$x! \to \sqrt{2\pi x} e^{-x} x^x \text{ as } x \to \infty. \tag{3.34}$$

Plugging this into the Poisson distribution gives

$$\begin{aligned}
&\frac{\lambda^{\lambda(1+\delta)}}{\sqrt{2\pi\lambda(1+\delta)} e^{-\lambda(1+\delta)} (\lambda(1+\delta))^{\lambda(1+\delta)}} e^{-\lambda} \\
&\frac{\lambda^{\lambda(1+\delta)}}{\sqrt{2\pi\lambda}(1+\delta)^{\frac{1}{2}} e^{-\lambda(1+\delta)} (\lambda(1+\delta))^{\lambda(1+\delta)}} e^{-\lambda} \\
&\frac{\lambda^{\lambda(1+\delta)} e^{-\lambda} e^{\lambda(1+\delta)} (1+\delta)^{-\frac{1}{2}} (\lambda(1+\delta))^{-\lambda(1+\delta)}}{\sqrt{2\pi\lambda}} \\
&\frac{e^{\lambda\delta}(1+\delta)^{-\lambda(1+\delta)-\frac{1}{2}}}{\sqrt{2\pi\lambda}}.
\end{aligned} \tag{3.35}$$

Then, we have

$$\begin{aligned}
\ln((1+\delta)^{\lambda(1+\delta)+\frac{1}{2}}) &= (\lambda(1+\delta) + \frac{1}{2}) \ln(1+\delta) \\
&= (\lambda + \frac{1}{2} + \delta)(\delta - \frac{\delta^2}{2} + \mathcal{O}(\delta^3)) \\
&\approx \lambda\delta - \lambda\frac{\delta^2}{2} + \frac{1}{2}\delta - \frac{1}{2}\frac{\delta^2}{2} + \delta^2 - \frac{\delta^3}{2} + \mathcal{O}(\delta^3)) \\
&= (\lambda + \frac{1}{2})\delta - (\lambda + \frac{1}{2})\frac{\delta^2}{2} + \delta^2 + \mathcal{O}(\delta^3)) \\
&\approx \lambda\delta - \lambda\frac{\delta^2}{2},
\end{aligned} \tag{3.36}$$

where the last approximation is justified since $\lambda \gg 1$. Hence, we have

$$(1+\delta)^{-\lambda(1+\delta)-\frac{1}{2}} = e^{\ln((1+\delta)^{-\lambda(1+\delta)-\frac{1}{2}})} \approx e^{-\lambda\delta+\lambda\frac{\delta^2}{2}}. \tag{3.37}$$

Plugging this back in the equation we obtained in (3.35) gives

$$\frac{e^{\lambda\delta}e^{-\lambda\delta+\lambda\frac{\delta^2}{2}}}{\sqrt{2\pi\lambda}} = \frac{e^{\lambda\frac{\delta^2}{2}}}{\sqrt{2\pi\lambda}}. \tag{3.38}$$

Now, we use $\delta = \frac{x-\lambda}{\lambda}$ and obtain

$$e^{\frac{(x-\lambda)^2}{2\lambda}}. \tag{3.39}$$

This is a Gaussian function with height 1, center λ and variance λ. Thus, the Poisson distribution can be approximated by a Gaussian for large values of n.

3.6.5. Implementation

Both the Poisson noise and the recombination noise have a Poisson distribution and can thus be approximated with a Gaussian distribution. Because the sampling period of DESHIMA (1/160 Hz = 6 ms) is much larger than the coherence time of the incoming photons, photon bunching can be approximated with a normal distribution as well. TiEMPO interprets the NEP as the variation in the KID power and used a normal distribution to simulate the fluctuations in the KID power. We took a standard deviation of

$$\sigma = NEP_{ph}\sqrt{\frac{1}{2}f_{sampling}}, \tag{3.40}$$

where $f_{sampling}$ is the sampling frequency and equals 160 Hz in DESHIMA. Before we sum the power over the bins to obtain the total power P_{MKID}, we need to add the photon noise to each bin. To this end, a Gaussian distribution is created using P_{bin} as a mean and the standard deviation is calculated using Equation 3.40. We take a random value from this distribution and add it to the bin power. Finally, we sum all bin powers to obtain the MKID power, and this is done for each channel.

$$P_{MKID} = \sum_{i=1}^{\#bins} P_{with\ noise,bin\ i} \tag{3.41}$$

It is important to note that the noise has to be added per bin instead of to the total power. If we use the total power and the equivalent bandwidth, we are approximating the filter as in Figure 3.17. In this approximation, the power is concentrated in the equivalent bandwidth, meaning that there is more power per frequency (the psd is larger). In equation (3.30), we see that this increases the photon bunching term, as the total power is the same but it is spread over a smaller bandwidth. Photon bunching can only happen between photons with the same frequency, explaining the increase in photon bunching if we have more photons of the same frequency [53]. In reality, the photons are distributed as the filter response, and not uniformly as the equivalent bandwidth approach assumes. Thus, we conclude that the most accurate way to model the noise, is to add it per bin and sum over those values.

3.7. Converting power to sky temperature

After we have computed the power that is received by the MKIDs, we want to relate this back to the original signal from the sky. We do this by expressing the received power in sky temperature: the physical temperature of a blackbody that would have the same intensity as the semitransparent sky. It is important to note that this definition is slightly different from the definition used in [54]. The commonly used Rayleigh-Jeans approximation for the sky temperature is only valid when $hf << k_BT$. In our case, as the sky temperature is approximately 275 K, the Rayleigh-Jeans limit holds, so we could use either the Rayleigh-Jeans or the Johnson-Nyquist formula for determining the sky temperature, as long as it is done consistently throughout TiEMPO

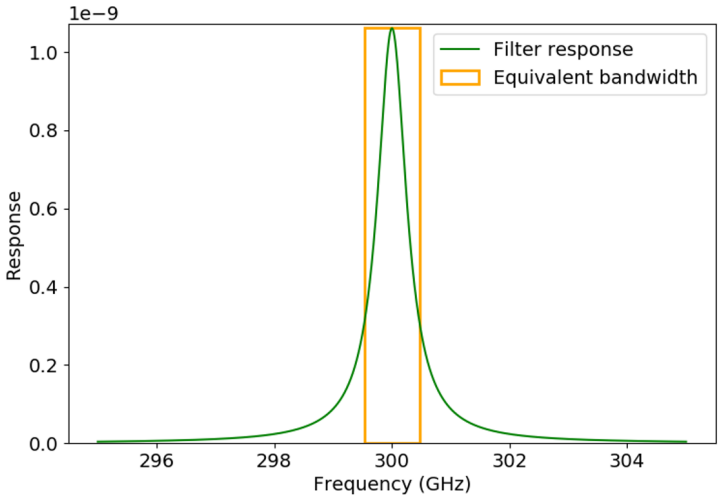

Figure 3.17: The filter response of the filter centered at 300 GHz, compared to its equivalent bandwidth. In the equivalent bandwidth approximation, the psd is taken to be higher in a more concentrated frequency domain, resulting in a larger photon bunching term in the NEP.

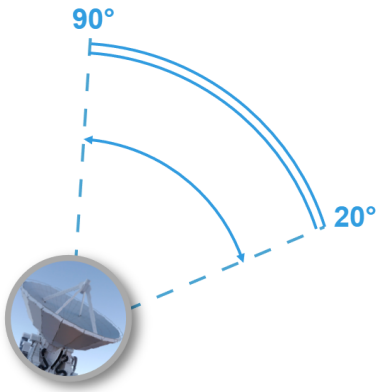

Figure 3.18: Illustration of a skydip experiment. The elevation of the telescope is varied from 90 to 20 degrees, obtaining a range of values for the sky temperature and the received power. This image is from Akira Endo (private communication).

and in the post-analysis. We chose to use the Johnson-Nyquist formula, which is given by

$$T_{sky} = \frac{hf}{k_B \, ln(\frac{hf}{psd+1})}, \tag{3.42}$$

where h is Planck's constant, f is the frequency, and psd is the power spectral density. In order to relate the KID power to the sky temperature, we did a skydip simulation in the DESHIMA simulator (see Section 3.5 for detailed information about the DESHIMA simulator). A skydip is a series of measurements in which the telescope 'dips' from a high elevation (pointing at zenith) to a low elevation (pointing almost horizontally), see Figure 3.18. When the elevation is lower, the telescope looks through a larger layer of atmosphere, increasing the opacity, and hence the power and the sky temperature, allowing us to construct a relationship between the two. In our experiment, we used elevation values between 20 and 90 degrees, where 90 degrees is at zenith. This gives us enough values to base the calibration on, and calculations with an elevation lower than 20 degrees are less accurate, because the curvature of the Earth is not taken into account in the DESHIMA simulator, as illustrated in Figure 3.19. Furthermore, we have taken into account the increase in optical depth with a decreasing elevation, but not the increased and elliptically shaped telescope beam (When the elevation decreases, the telescope beam tilts, while the atmosphere screen keeps the same orientation, resulting in an increased and elliptically shaped cross-section of the telescope beam where it passes the atmosphere screen).

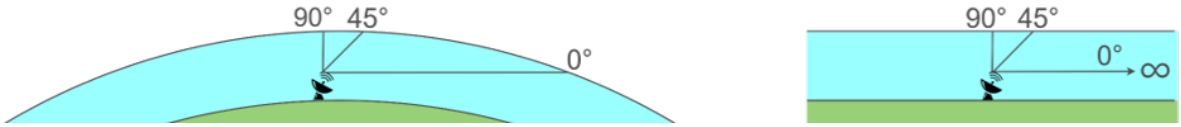

Figure 3.19: Illustration of a skydip experiment. On the left, the curvature of the earth is taken into account, whereas on the right, it is not. We see that for large elevations (45 to 90 degrees) the difference in the path length through the atmosphere is minimal, whereas this difference becomes much larger with small elevations, eventually approaching infinity when the elevation approaches zero.

Hence, we are integrating the precipitable water vapor over a too small range of atmosphere values for low elevations. We construct the power from the psd using the binning as explained before (see Sections 3.6.1 and 3.6.5), and the sky temperature is obtained from psd_{sky} using Equation (3.42). However, in addition to integrating psd_{sky} over the filter response, the atmospheric transmission needs to be integrated as well [54]. The reason for this is that the bandwidth of a channel is finite, which implies that light of different frequencies comes in. Each frequency has a different atmospheric transmission value, so taking one value of the atmospheric transmission per filter is not accurate (see Figure 3.20 or [3] for an animation containing all frequencies).

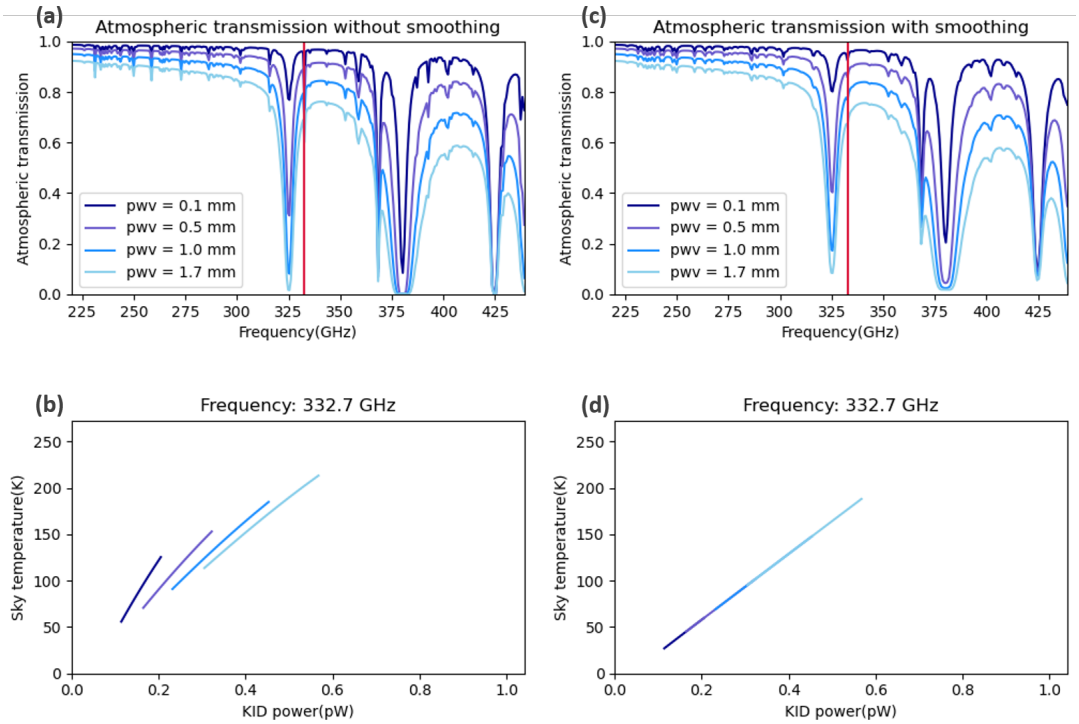

Figure 3.20: Comparison between the atmospheric transmission with and without smoothing. **a.** Unsmoothed atmospheric transmission plotted against the frequency for different values of the precipitable water vapor. The data were obtained using [15], [16]. **b.** The sky temperature versus the KID power for different values of the precipitable water vapor. The data are obtained from the DESHIMA simulation (see Section 3.5), where the elevation was varied from 20 to 90 degrees. We see that the curve is not only dependent on the elevation, but also on the precipitable water vapor. **c.** Smoothed atmospheric transmission plotted against the frequency for different values of the precipitable water vapor. The data were obtained using [15], [16].**d.** The sky temperature versus the KID power for different values of the precipitable water vapor.

[3] https://youtu.be/GGf0Osv4HM4

We see that the data lie on the same curve for different values of the precipitable water vapor when the atmospheric transmission is smoothed, showing an injective relation (only one KID power value corresponds to each sky temperature value) between the KID power and the sky temperature, so the sky temperature can be determined unambiguously if the KID power is known. The power and sky temperature data are interpolated for each channel and saved in the model. TiEMPO reuses these interpolation curves, so that they only need to be created once.

3.8. Computational challenges

TiEMPO simulates 8-11 hours of observation with the ASTE telescope. The size of the data is therefore large and this poses some computational challenges.

First of all, the atmosphere data generated from ARIS is approximately 4 GB in total. The reason for this large datasize is that we need a very long phasescreen, for example $10 \cdot 8 \cdot 3.600 = 288$ km for an 8-hour observation with a wind speed of 10 m/s. If we would store this data in one file, loading in this file would take very long. Hence, we have chosen to use 40 smaller files instead. TiEMPO is made so that only the necessary files are loaded in, preventing unnecessarily long computation time for shorter observation simulations.

Furthermore, the number of timesteps in the model is very large. DESHIMA observes with a frequency of 160 Hz, which means that we need $8 \cdot 3600 \cdot 160 = 4.6$ million timesteps for an 8-hour observation. Counting the 5 different pwv values we take in each timestep, this results in 23 million sky temperature values that need to be computed. We chose to operate TiEMPO on the server of the Terahertz Sensing Group. This enables us to make it run parallel, using 30 cores. Instead of executing the timesteps consecutively, TiEMPO now executes multiple timesteps at the same time, which is possible since the timesteps are independent of each other, see Figure 3.21.

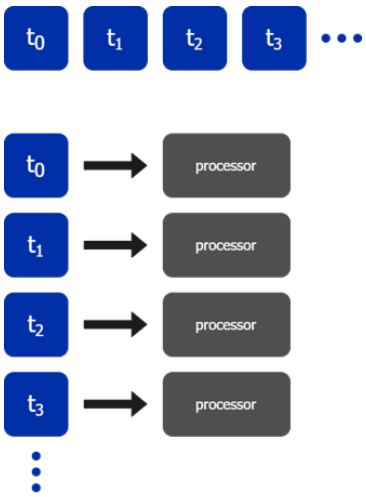

Figure 3.21: Schematic image of the parallel computation used in the DESHIMA model. Instead of executing the timesteps consecutively, the model executes multiple timesteps at the same time (this is possible, because the timesteps are independent of eachother).

4

Early results of full simulations

This chapter shows various early results of the full TiEMPO simulation. It shows the time signal TiEMPO produces and compares simulation data to observation data by means of the power spectral density and noise equivalent flux density. The observation data used in this chapter are obtained by DESHIMA. If TiEMPO is capable of accurately simulating DESHIMA, we are confident that it will be powerful in predicting DESHIMA 2.0.

4.1. Sky temperature

Figure 4.1 shows the sky temperature in K plotted against the time in minutes for an observation performed by DESHIMA and a simulation by TiEMPO, with similar telescope elevation and weather conditions. The blue signal shows the raw observation data, in which a drift of the sky temperature is present. The green signal shows the observation data without this drift, and the orange signal shows the simulation data. Qualitatively, the plots show excellent agreement: they consist of high-frequency fluctuations with a small amplitude, that we suspect are caused by photon and recombination noise; and low-frequency fluctuations with a larger amplitude, that we suspect are caused by atmospheric noise. Both the low-frequency and the high-frequency fluctuations seem to have a smaller amplitude in the simulation data with the high-frequency fluctuation amplitude differing with a factor of approximately 1.6. This is further analysed in the next Section.

The drift in the sky temperature values of the observation data is remarkable. We suspect that the value of the precipitable water vapor that is given in the observation data is the value measured at the beginning of the experiment. Hence, it is possible that the average value of the precipitable water vapor dropped over the course of the experiment, causing a decrease in the sky temperature. In this simulation, TiEMPO assumed a constant average value of the precipitable water vapor.

The sky temperature range of the observation (62.5-77 K) corresponds to pwv values ranging from 1.27 mm to 1.75 mm, approximately (calculated using desim). The pwv value of 1.7 mm, which was used in the simulation, corresponds to a sky temperature of 78.58 K. In the plot of the simulation data, we see that it indeed fluctuates around this value.

4.2. Power spectral density

The data from the previous Section has also been used in this Section to obtain the power spectral density. The power spectral density helps us to determine if the noise in both signals has the same characteristics, which is not immediately clear from studying time signals. Figure 4.2 shows the power spectral density in Jy^2/Hz

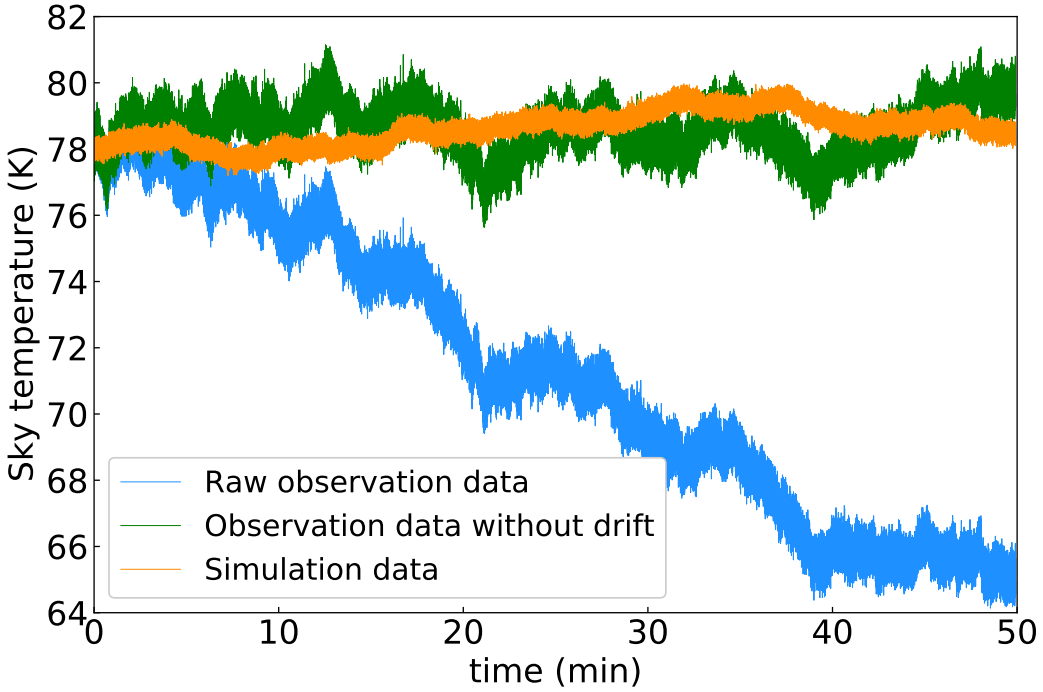

Figure 4.1: Sky temperature in K plotted against the time in minutes for a real observation of DESHIMA and a simulation made by TiEMPO for the 350 GHz channel. The observation data was obtained from a still sky measurement (measurement in which the telescope does not move) with an elevation of 88 degrees. The duration of the experiment was 50 minutes. The precipitable water vapor was 1.72 mm and the windspeed was 1.13 m/s. The simulation data was produced with an elevation of 90 degrees, an average precipitable water vapor of 1.7 mm, and a windspeed of 10 m/s. The blue signal shows the raw observation data, in which a drift of the sky temperature is present. The green signal shows the observation data without this draft, made by subtracting a linear relation from the signal made with linear regression on the original signal. The orange signal shows the simulation data.

plotted against the frequency in Hz for the TiEMPO simulation and DESHIMA observation, shown in orange and blue, respectively. The psd is made for the filter with a center frequency of 350 GHz. The flat level S_F of the signals is shown by the dashed lines.

In this Figure, we observe that the psd of TiEMPO reproduces key characteristics from the psd of the DESHIMA observation data. First of all, both spectra show a white noise spectrum from frequencies starting at 1 Hz. This originates from photon and recombination noise, see Section 3.6.2. Secondly, for frequencies lower than 1 Hz, the spectra roughly follow a $1/f$-shape, which is caused by atmosphere fluctuations, see Section 3.3. This indicates that the atmospheric model of TiEMPO, which is based on the ARIS atmosphere model and the newly introduced conversion of EPL to pwv (Section 3.3.1), is a good representation of real atmospheric fluctuations.

We also observe differences between the spectra. The white noise levels differ with a factor of approximately 2.6. In Section 4.1, we saw the same difference of $\sqrt{2.6} \approx 1.6$. Furthermore, the low-frequency noise differs by a factor of 10^4. We expect that this is due to the exact properties of each filter channel of the spectrometer chip, that have not been taken into account in TiEMPO.

Recently, Kaushal Marthi has used TiEMPO for a more detailed investigation on reproducing DESHIMA observation data (for more details, see the report of Kaushal Marthi, in preparation at the time of writing). In his work, he takes into account the laboratory-measured optical efficiency and filter bandpass-characteristics of all channels. Furthermore, the RMS fluctuation of the Extra Pathlength in the ARIS atmosphere model was increased from 50 to 150 μm. Some of his most succesful results are shown in Figure 4.3. In this Figure, the power spectral density of the KID response is plotted. Again, we observe that the slopes are in excellent agree-

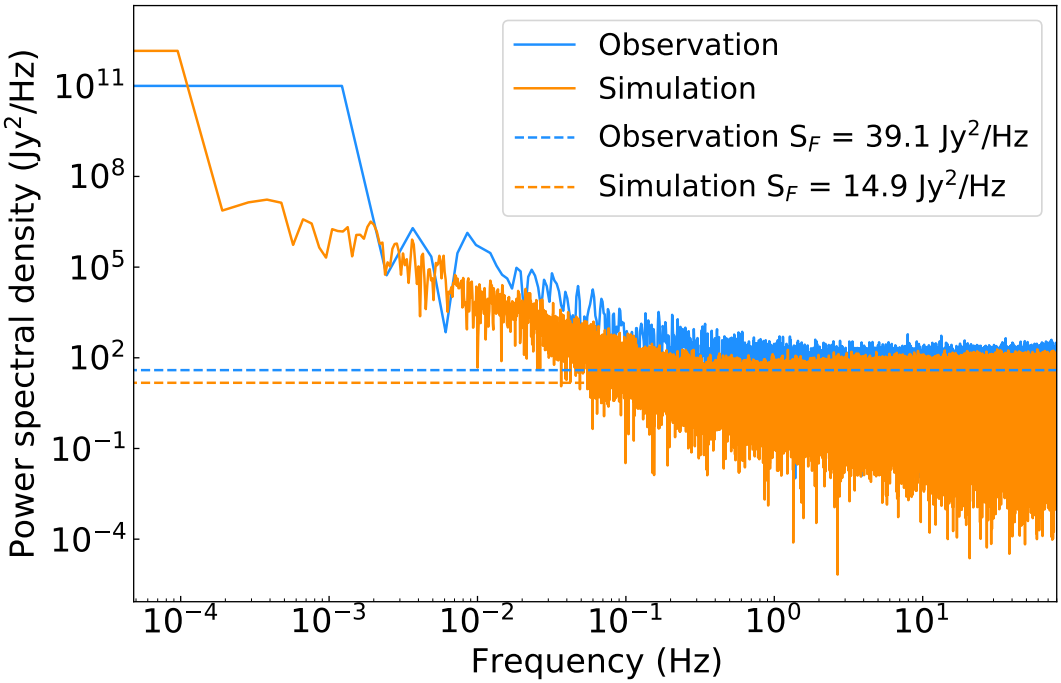

Figure 4.2: The power spectral density in Jy^2/Hz plotted against the frequency in Hz (this data was obtained by Yannick Roelvink, private communications). The orange curve shows the signal obtained from TiEMPO, and the blue line shows the signal from the DESHIMA observation. The DESHIMA observation is a still sky measurement (measurement in which the telescope does not move) done with an elevation of 88 degrees. The duration of the experiment was 50 minutes, the precipitable water vapor was 1.72 mm, and the windspeed was 1.13 m/s. The TiEMPO simulation was performed with an elevation of 90 degrees, an average precipitable water vapor of 1.7 mm, and a windspeed of 10 m/s. The orange and blue dashed lines show the flat level of the DESHIMA observation and the TiEMPO simulation, respectively.

ment. The difference in white noise level is now almost eliminated. These results show that incorporating the measured properties of all channels in TiEMPO and choosing the right atmosphere parameters results in a much better match between observation and simulation data, which is a promising result for TiEMPO.

4.3. Noise Equivalent Flux Density

Next to the psd, we also want to study the instrument sensitivity that TiEMPO predicts. The sensitivity of DESHIMA is expressed in Noise Equivalent Flux Density, or NEFD. The NEFD is the minimal flux density of the signal needed so that it equals the noise flux density; the lower the NEFD, the more sensitive the instrument.

4.3.1. Expression of the NEFD

In order to calculate the NEFD, we first determine the flux density. The flux density is given by

$$F_f = \frac{psd}{A_e \eta_{atm}}, \tag{4.1}$$

where F_f is the flux density in Jy, A_e is the effective aperture area in m^2, defined by $A_e = \eta_a A_p$, where η_a is the antenna efficiency and is given in 3.17. Combining equation 4.1 and 3.17 gives

$$F_f = 10^{26} \cdot \frac{2}{A_e \eta_{atm}} \frac{hf}{e^{\frac{hf}{k_B T_{sky}}} - 1}. \tag{4.2}$$

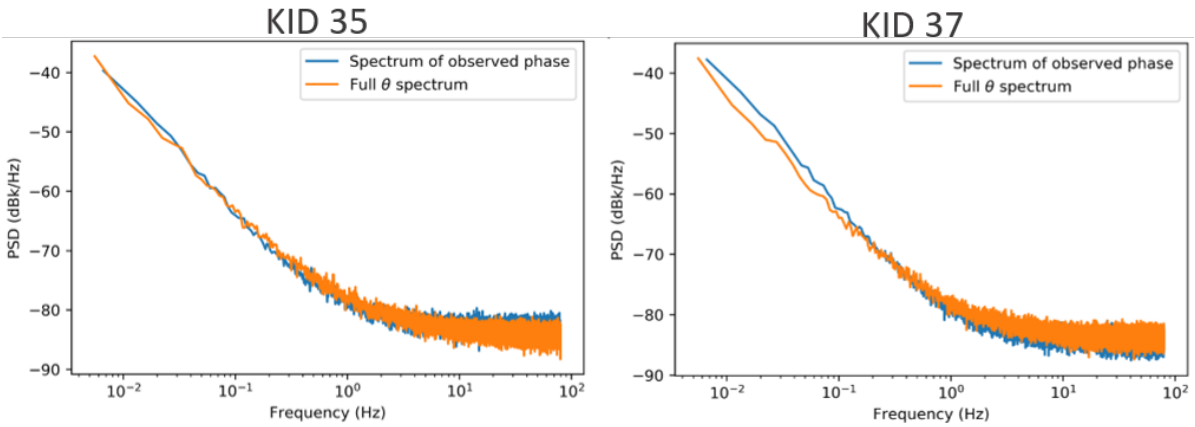

Figure 4.3: The Power Spectral Density in dBk/Hz plotted against the frequency in Hz for KID 35 and 37.

The factor 10^{26} is multiplied to obtain a result in Jansky. Using (4.2), the T_{sky} output of TiEMPO is converted to the flux density. Subsequently, the power spectral density S_F of this signal is derived in Jy^2/Hz, and from this power spectral density, the NEFD is calculated as

$$NEFD = \frac{\sqrt{S}}{\sqrt{2}}, \tag{4.3}$$

where S is the noise power spectral density in $W/\sqrt{Hz}$.

4.3.2. Results

We have calculated the NEFD in 3 different ways: with TiEMPO data and smoothed atmospheric transmission, with TiEMPO data and raw (unsmoothed) atmospheric transmission, and with static model desim data, which uses the raw atmospheric transmission (see Section 3.5). Figure 4.4 shows the resulting NEFD curves, accompanied by DESHIMA observation data of the luminous infrared galaxy VV 114 and the luminous red giant IRC+10216 [22] [55].

We see that the green and orange curve match very well. They are overlapping over the whole frequency range and have the same peak at approximately 368 GHz. The green curve was made using static model desim, which determines the NEFD directly from the KID power. The orange curve uses TiEMPO data, which includes the atmospheric noise, photon noise, recombination noise, the filter shape of the frequency channels and a conversion from KID power to sky temperature. This result suggests that the atmospheric modeling, the noise modeling, the filter shape modeling and the conversion KID power to sky temperature conversion represent the process realistically.

As we saw in Section 3.7, using the raw atmospheric transmission gives less accurate results. The curve of the smoothed atmospheric transmission is indeed slightly different than the other 2 curves, and is the closest to the DESHIMA observation data, indicating that the filter shape and the smoothing of the atmospheric transmission are modeled realistically. The curves differ the most around the peak at 368 GHz and at frequencies higher than 375 GHz. The cause of this difference is that in these parts of the spectrum, the atmospheric transmission changes rapidly (see Figure 1.4), causing the smoothing of the atmospheric transmission to have a larger effect.

All curves underestimate the NEFD in the low frequency part of the graph (332-345 GHz) and overestimate the NEFD in the high frequency part of the graph (354-377 GHz). This can be explained as follows. First of all, the quasioptical bandfilter in the optics of the DESHIMA instrument reduces the optical efficiency on the boundaries of the band (see Figure 4.5). For the low frequencies, this effect is very large, explaining the higher NEFD of the observation data. For the high frequencies, this effect is smaller. In this simulation, TiEMPO assumed an average pwv value of 1.7 mm, which is larger than the pwv at the moment of the observations.

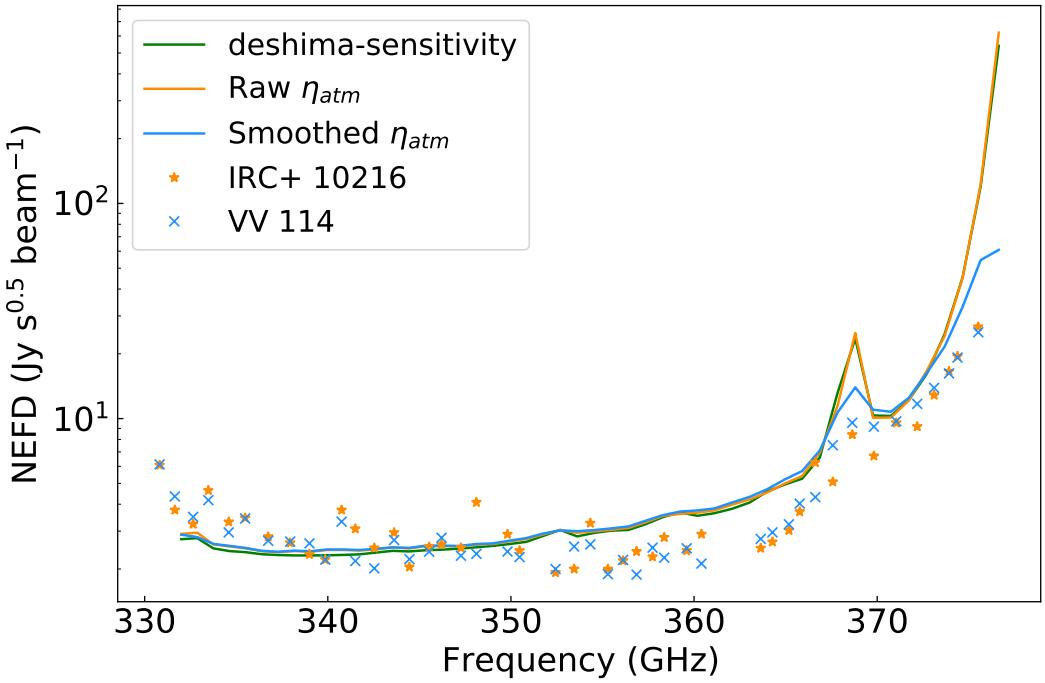

Figure 4.4: The Noise Equivalent Flux Density (NEFD) in Jy $s^{1/2}$/beam versus the frequency in GHz. The blue curve shows the NEFD calculated with the Johnson-Nyquist power and the smoothed atmospheric transmission (see Section 3.7 for an explanation about the smoothed atmospheric transmission). The orange curve shows the NEFD calculated with the Johnson-Nyquist power and the raw (unsmoothed) atmospheric transmission, and the green curve shows the NEFD calculated with the static model desim. The blue crosses and orange stars show DESHIMA observation data for the VV114 and IRC 10216 galaxies, respectively.

Therefore, the predicted NEFD is higher than the observed NEFD for the high frequencies, where the decrease in instrument efficiency does not compensate for that.

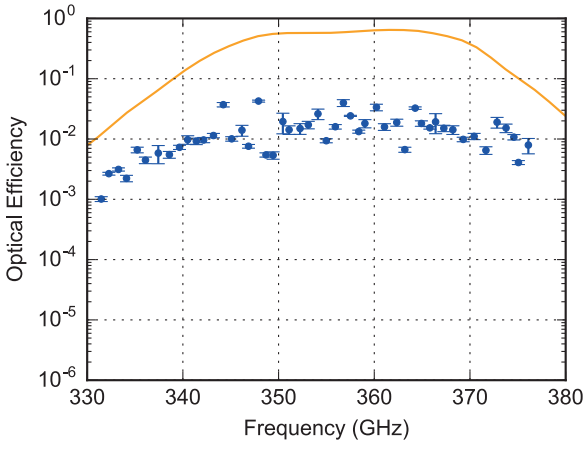

Figure 4.5: The Optical Efficiency plotted against the Frequency in GHz. The orange line denotes the transmission of the quasioptical filter, whereas the blue points denote the Optical Efficiency for each filter channel. This figure is taken from [10].

5

Conclusions and future prospects

5.1. Conclusions

In this work, we created the Time-dependent End-to-end Model for Post-process Optimization (TiEMPO). In comparison to similar models, TiEMPO makes two major improvements. First of all, TiEMPO uses ARIS, which models a spatially as well as dynamically varying atmosphere [1]. Secondly, TiEMPO is the first end-to-end model of the DESHIMA process, enabling it to produce very realistic observation simulations.

We have made a few benchmark comparisons between the time-domain signal produced by TiEMPO and on-sky data taken by DESHIMA in 2017. A comparison between the time signals shows excellent qualitative agreement, indicating realistic modeling of the atmospheric fluctuations, a Gaussian near-field beam, photon noise and recombination noise. In addition, it suggests that our newly found conversion between KID power and sky temperature is realistic.

A comparison between the power spectral densities of both signals further supports this result, showing (1) the white noise characteristics we expect from photon and recombination noise, and (2) the $1/f$-slope for lower frequencies we expect from atmosphere fluctuations. We do observe a factor of 2.6 difference in the flat level of the power spectral densities, which is due to channel-to-channel variation in the optical efficiency and filter bandpass-characteristics. This difference is eliminated in the analyses of Kaushal Marthi, in which channel-to-channel variation is taken into account.

The Noise Equivalent Flux Density of the TiEMPO simulation resembles the observation data well. We observed that the results using a smoothed atmospheric transmission resemble the observation data the closest, validating this method and our approximation of the filter shape with a Lorentzian curve. The small differences between the observation and simulation data can be explained by the different weather conditions and the frequency-dependenct optical efficiency.

The overall excellent agreement between observation and simulation data shows the potential of TiEMPO as a powerful tool for optimizing the software and observing strategies of DESHIMA 2.0. TiEMPO allows us to test atmosphere removing software, to study the effect of different weather conditions and to evaluate the performance of different observing techniques. In addition, TiEMPO is usable for the original DESHIMA instrument and of its successor, DESHIMA 2.0. It can even be used to test similar spectrometers, like a grating spectrometer, and on different telescopes, such as the promising 50m-aperture AtLAST/LST telescope [3] [4].

5.2. Future prospects

The results shown in this thesis are made with the first simulations of TiEMPO. In the future, more simulations need to be made to test TiEMPO more thoroughly. Yannick Roelvink is simulating with TiEMPO for his bachelor project, and will test it with different input parameters. Next to that, he will simulate the detection of SMGs with DESHIMA 2.0 on the ASTE telescope using TiEMPO.

In this first version of TiEMPO, many properties of the DESHIMA instrument are approximated for simplicity, such as the filter response, the near-field beam, and the optical efficiency. TiEMPO can be made more accurate if these approximations are changed to simulated or measured values of the instrument. Kaushal Marthi has made a start with this, simulating the optical efficiency and filter bandpass-characteristics for each channel. Next to that, he has changed a parameter in the atmosphere simulation, improving his results. His early results discussed in this thesis are very promising.

In addition, we observed a drift in the sky temperature data of the DESHIMA observations, possibly caused by a drift in the precipitable water vapor. As a sky temperature drift occurs not only because of pwv drifts but can also be caused by variations in the elevation during source-tracking, it is recommendable to add a pwv drift to the atmosphere data in TiEMPO.

Finally, in addition to DESHIMA simulations, TiEMPO can also be used in other studies. For example, Stan Zaalberg is using TiEMPO in his bachelor project to model the Sunyaev-Zeldovich effect (the distortion of CMB radiation in galaxy clusters). This shows the wide applicability of TiEMPO. In the future, TiEMPO can be used to test new observation techniques and to study astronomical phenomena.

Appendices

A. Downloading TiEMPO

The code of TiEMPO can be downloaded at GitHub[1]. In order to run the model, python 3 is required.
Required packages: NumPy, Matplotlib, math, time, SciPy, sys, os, multiprocessing, Joblib, progress, pandas, copy, base64, mpl_toolkits, glob

[1] https://github.com/EsmeeHuijten/DESHIMAmodel

B. Parameters used in TiEMPO in this thesis

Table 1: An overview of the parameters that were used in the TiEMPO simulations in this thesis. In italics, the file in which the parameter is located is denoted.

Parameter	DESHIMA	DESHIMA 2.0
main.py		
F_min	$332 \cdot 10^9$	$220 \cdot 10^9$
num_bins	1500	1500
spec_res	300	500
num_filters	49	347
windspeed	10	10
beam_radius	5.	5.
useDESIM	1	1
inclAtmosphere	1	1
luminosity	13.7	13.7
redshift	4.43	4.43
linewidth	600	600
EL	60.-90.	60.
pwv_0	1.	1.
D1	1	0
use_desim.py (init)		
eta_M1_spill	0.99	0.99
eta_M2_spill	0.90	0.90
n_wo_mirrors	2.	4.
window_AR	False	True
eta_co	0.65	0.65
eta_lens_antenna_rad	0.81	0.81
eta_circuit	$0.35 \cdot 0.1$	0.35
eta_IBF	0.6	0.6
KID_excess_noise_factor	1.0	1.1
Tb_cmb	2.725	2.725
Tp_amb	273.	273.
Tp_cabin	290.	290.
Tp_co	4.	4.
Tp_chip	0.12	0.12
use_desim.py (transmit_through_DESHIMA, obt_data and calcT_psd_P methods)		
theta_maj	31.4 · np.pi/180./60./60.	use_desim.D2HPBW(F_bins_Lor)
theta_min	22.8 · np.pi/180./60./60.	use_desim.D2HPBW(F_bins_Lor)
eta_mb	0.34	self.eta_mb_ruze(F=F_bins_Lor, LFlimit=0.8, sigma=37e-6) · 0.9

C. Project Output

1. This BSc report and final presentation
2. The modeling and key results in this report have been accepted as a poster presentation at the international conference SPIE Astronomical Telescopes + Instrumentation, San Diego, California, United States, 13-18 December 2020, as:
   Modeling of the DESHIMA spectrometer for validating the software and calibration method
   Esmee Huijten*, Yannick Roelvink, Kaushal Marthi, Stan Zaalberg, Akio Taniguchi, Tom Bakx, Jochem J. A. Baselmans, Kah Wuy Chin, Robert Huiting, Kenichi Karatsu, Alejandro Pascual Laguna, Yoichi Tamura, Tatsuya Takekoshi, Stephen J. C. Yates, Maarten van Hoven, and Akira Endo*
3. The TiEMPO model is made public as a python library on the open-source repository GitHub at https://github.com/EsmeeHuijten/DESHIMAmodel
   (a) We plan to publish TiEMPO on the open repository of the DESHIMA collaboration at https://github.com/deshima-dev
   (b) The repository includes a detailed "README" file that explains how to use the program
4. Intermediate reports on the internal wikipage ('kibela') of the DESHIMA collaboration
   (a) "README DESHIMAmodel"
   (b) "Obtaining a pwv map from ARIS"
   (c) "Midway presentation Esmee"
   (d) "Atmosphere model ARIS"
5. Public Outreach
   Presentations to the general public at the TU Delft Open House Days on 6 and 7 March 2020 (2 days x 3 times)

Acknowledgements

First and foremost, I would like to thank Akira Endo, for his great support and commitment during my project. Thank you for your encouragement and your trust, even giving me the opportunity to attend an international conference. You gave me invaluable advice on my project, but also on presenting and writing. In the small glimpse of the academic community I've had, you are one of the most enthusiastic, optimistic and dedicated researchers I know and this was a great source of motivation and inspiration for me.

Secondly, I would like to thank Akio Taniguchi, Yoshiharu Asaki, Kenichi Karatsu, Tom Bakx, Yannick Roelvink, Kaushal Marthi, Jochem Baselmans, Kah Wuy Chin, Robert Huiting, Alejandro Pascual Laguna, Yoichi Tamura, Tatsuya Takekoshi, Stephen Yates, Maarten van Hoven and Aurèle Adam for providing me with components for TiEMPO, knowledge about DESHIMA and astronomy in general, and helping me to improve TiEMPO with your suggested improvements. Without you, TiEMPO would not be in existence!

I would also like to express my appreciation to the whole THz Sensing Group of the TU Delft, for making me feel so included. You really treated me as a colleague, inviting me for lunch every day, inviting me for all the group activities, having a nice chat during the coffee breaks and taking the time to listen and ask critical questions during my project updates and presentations.

Lastly, I would like to thank my boyfriend, parents, housemates, and study friends. Cees, I thank you for all your love and support during my Bachelor End Project, but also for being the most critical person around and helping me strive for the best version of my project. Mom, dad, thank you for always listening to my practice presentations and for having full trust in me, even if you don't completely understand my project. Lotte, Xavier, Claudio and Asiya, thank you for tirelessly listening to my practice presentations, my doubts, my complaints, and my ideas. Sam, Stephan, Ilse, Angeline and Tim, thank you for supporting me throughout my bachelor studies, being there for me and brightening my day time after time. As my time in Delft is drawing to a close, I realise more and more how much I will miss you. Thank you for making my years in Delft enjoyable, memorable, and nothing short of amazing!

Bibliography

[1] Y. Asaki, H. Sudou, Y. Kono, A. Doi, R. Dodson, N. Pradel, Y. Murata, N. Mochizuki, P. G. Edwards, T. Sasao, *et al.*, *Verification of the effectiveness of vsop-2 phase referencing with a newly developed simulation tool, aris,* Publications of the Astronomical Society of Japan **59**, 397 (2007).

[2] A. Endo, K. Karatsu, Y. Tamura, T. Oshima, A. Taniguchi, T. Takekoshi, S. Asayama, T. J. Bakx, S. Bosma, J. Bueno, *et al.*, *First light demonstration of the integrated superconducting spectrometer,* Nature Astronomy **3**, 989 (2019).

[3] P. Klaassen, T. Mroczkowski, S. Bryan, C. Groppi, K. Basu, C. Cicone, H. Dannerbauer, C. De Breuck, W. J. Fischer, J. Geach, E. Hatziminaoglou, W. Holland, R. Kawabe, N. Sehgal, T. Stanke, and E. van Kampen, *The atacama large aperture submillimeter telescope (atlast),* https://ui.adsabs.harvard.edu/abs/2019BAAS...51g..58K (2019).

[4] R. Kawabe, K. Kohno, Y. Tamura, T. Takekoshi, T. Oshima, and S. Ishii, *New 50-m-class single-dish telescope: Large submillimeter telescope (lst),* https://ui.adsabs.harvard.edu/abs/2016SPIE.9906E..26K (2016).

[5] C. Kulesa, *Terahertz spectroscopy for astronomy: From comets to cosmology,* IEEE Transactions on Terahertz Science and Technology **1**, 232 (2011).

[6] Clinuvel, *Understanding the electromagnetic spectrum,* https://www.clinuvel.com/photomedicine/physics-optics-skin/electromagnetic-spectrum/understanding-the-electromagnetic-spectrum (2018).

[7] N. Erickson, G. Narayanan, R. Goeller, and R. Grosslein, *Asp conference series, from z-machines to alma:(sub) millimeter spectroscopy of galaxies, eds,* Baker, Glenn, Harris, Mangum, and Yun **375**, 71 (2007).

[8] G. J. Stacey, *Thz low resolution spectroscopy for astronomy,* IEEE Transactions on Terahertz Science and Technology **1**, 241 (2011).

[9] L. McNish, *Rasc calgary centre - cosmological redshift,* https://calgary.rasc.ca/redshift.htm (2012).

[10] A. Endo, K. Karatsu, A. P. Laguna, B. Mirzaei, R. Huiting, D. J. Thoen, V. Murugesan, S. J. Yates, J. Bueno, N. van Marrewijk, *et al.*, *Wideband on-chip terahertz spectrometer based on a superconducting filterbank,* arXiv preprint arXiv:1901.06934 (2019).

[11] H. Ezawa, R. Kawabe, K. Kohno, and S. Yamamoto, *The atacama submillimeter telescope experiment (aste),* in *Ground-based Telescopes*, Vol. 5489 (International Society for Optics and Photonics, 2004) pp. 763–772.

[12] A. P. Laguna, K. Karatsu, A. Neto, A. Endo, and J. Baselmans, *Wideband sub-mm wave superconducting integrated filter-bank spectrometer,* in *2019 44th International Conference on Infrared, Millimeter, and Terahertz Waves (IRMMW-THz)* (IEEE, 2019) pp. 1–2.

[13] A. Endo, *Wp1.2 deshima 2.0 hardware requirements,* https://deshima.kibe.la/shared/entries/ff96eb1f-ef80-41e2-adf8-178769a72e3f (2018).

[14] Y. Sewnarain Sukul, *Principal component analysis on atmospheric noise measured with an integrated superconducting spectrometer,* Master's thesis, Delft University of Technology (2019), http://resolver.tudelft.nl/uuid:a75fde14-e7fb-401c-9c47-2f954fc5e70c.

[15] Almascience, *Atmosphere model,* https://almascience.eso.org/about-alma/atmosphere-model (unknown).

[16] J. Cernicharo, *Atm: a program to compute atmospheric transmission between 0-1000 ghz,* Internal Rep. Institut de Radioastronomie Millimétrique (IRAM) (1985).

[17] J. Baselmans, *Kinetic inductance detectors,* Journal of Low Temperature Physics **167**, 292 (2012).

[18] A. Taniguchi and T. Ishida, *De:code,* https://github.com/deshima-dev/decode (2019).

[19] Y. Gong, A. Cooray, M. Silva, M. G. Santos, J. Bock, C. M. Bradford, and M. Zemcov, *Intensity mapping of the [c ii] fine structure line during the epoch of reionization,* The Astrophysical Journal **745**, 49 (2011).

[20] C. K. Walker, *Terahertz astronomy* (Crc Press, 2015).

[21] *How [cii] 158 micron emission is produced in photodissociation regions (pdrs),* https://www.youtube.com/watch?v=SoZjymOsvsE (2013).

[22] C. D. Wilson, G. R. Petitpas, D. Iono, A. J. Baker, A. B. Peck, M. Krips, B. Warren, J. Golding, A. Atkinson, L. Armus, *et al.*, *Luminous infrared galaxies with the submillimeter array. i. survey overview and the central gas to dust ratio,* The Astrophysical Journal Supplement Series **178**, 189 (2008).

[23] K. M. C. M. Wong, T., *"on-the-fly" mapping with the mopra telescope,* https://www.atnf.csiro.au/news/newsletter/oct04/On_the_Fly_Mapping.htm (unknown).

[24] D. H. Hughes, S. Serjeant, J. Dunlop, M. Rowan-Robinson, A. Blain, R. G. Mann, R. Ivison, J. Peacock, A. Efstathiou, W. Gear, *et al.*, *High-redshift star formation in the hubble deep field revealed by a submillimetre-wavelength survey,* Nature **394**, 241 (1998).

[25] C. M. Casey, D. Narayanan, and A. Cooray, *Dusty star-forming galaxies at high redshift,* Physics Reports **541**, 45 (2014).

[26] L. Tacconi, R. Genzel, I. Smail, R. Neri, S. Chapman, R. Ivison, A. Blain, P. Cox, A. Omont, F. Bertoldi, *et al.*, *Submillimeter galaxies at z˜ 2: Evidence for major mergers and constraints on lifetimes, imf, and co-h2 conversion factor,* The Astrophysical Journal **680**, 246 (2008).

[27] M. Schmidt, *The rate of star formation.* The Astrophysical Journal **129**, 243 (1959).

[28] J. Hodge, A. Karim, I. Smail, A. Swinbank, F. Walter, A. Biggs, R. J. Ivison, A. Weiss, D. Alexander, F. Bertoldi, *et al.*, *An alma survey of submillimeter galaxies in the extended chandra deep field south: source catalog and multiplicity,* The Astrophysical Journal **768**, 91 (2013).

[29] T. J. Bakx, S. Eales, M. Negrello, M. Smith, E. Valiante, W. Holland, M. Baes, N. Bourne, D. Clements, H. Dannerbauer, *et al.*, *The herschel bright sources (herbs): sample definition and scuba-2 observations,* Monthly Notices of the Royal Astronomical Society **473**, 1751 (2018).

[30] M. Bonato, M. Negrello, Z.-Y. Cai, G. De Zotti, A. Bressan, A. Lapi, C. Gruppioni, L. Spinoglio, and L. Danese, *Exploring the early dust-obscured phase of galaxy formation with blind mid-/far-infrared spectroscopic surveys,* Monthly Notices of the Royal Astronomical Society **438**, 2547 (2014).

[31] J. Kamenetzky, N. Rangwala, J. Glenn, P. Maloney, and A. Conley, *Relations with co rotational ladders of galaxies across the herschel spire archive,* The Astrophysical Journal **829**, 93 (2016).

[32] P. A. Ade, N. Aghanim, M. Arnaud, M. Ashdown, J. Aumont, C. Baccigalupi, A. Banday, R. Barreiro, J. Bartlett, N. Bartolo, *et al.*, *Planck 2015 results-xiii. cosmological parameters,* Astronomy & Astrophysics **594**, A13 (2016).

[33] A. Endo and A. Taniguchi, *desim,* https://github.com/deshima-dev/desim (2019).

[34] A. Thompson, J. Moran, and G. Swenson Jr, *Interferometry and synthesis in radio astronomy, thompson ri, eisenstein d., fan x., rieke m., kennicutt rc, 2007,* ApJ **657**, 669 (2001).

[35] A. Dravskikh and A. Finkelstein, *Tropospheric limitations in phase and frequency coordinate measurements in astronomy,* Astrophysics and Space Science **60**, 251 (1979).

[36] Y. Asaki, M. Saito, R. Kawabe, K.-i. Morita, Y. Tamura, and B. Vila-Vilaro, *Alma memo no. 535 simulation series of a phase calibration scheme with water vapor radiometers for the atacama compact array,* NRAO (2005).

[37] A. Gurvich, B. Koprov, L. Tsvang, and A. Yaglom, *Atmospheric Turbulence and Radio Wave Propagation* (Nauka, Moscow, 1967).

[38] U. Frisch and A. N. Kolmogorov, *Turbulence: the legacy of AN Kolmogorov* (Cambridge university press, 1995).

[39] R. Giovanelli, J. Darling, C. Henderson, W. Hoffman, D. Barry, J. Cordes, S. Eikenberry, G. Gull, L. Keller, J. Smith, *et al.*, *The optical/infrared astronomical quality of high atacama sites. ii. infrared characteristics,* Publications of the Astronomical Society of the Pacific **113**, 803 (2001).

[40] S. Matsushita, Y. Asaki, E. B. Fomalont, K.-I. Morita, D. Barkats, R. E. Hills, R. Kawabe, L. T. Maud, B. Nikolic, R. P. Tilanus, *et al.*, *Alma long baseline campaigns: Phase characteristics of atmosphere at long baselines in the millimeter and submillimeter wavelengths,* Publications of the Astronomical Society of the Pacific **129**, 035004 (2017).

[41] E. K. Smith and S. Weintraub, *The constants in the equation for atmospheric refractive index at radio frequencies,* Proceedings of the IRE **41**, 1035 (1953).

[42] S. Paine, *The am atmospheric model SMA technical memo #152*, Smithsonian Astrophysical Observatory (2019).

[43] M. Bevis, S. Businger, S. Chiswell, T. A. Herring, R. A. Anthes, C. Rocken, and R. H. Ware, *Gps meteorology: Mapping zenith wet delays onto precipitable water,* Journal of applied meteorology **33**, 379 (1994).

[44] M. R. Moldover, J. M. Trusler, T. Edwards, J. B. Mehl, and R. S. Davis, *Measurement of the universal gas constant r using a spherical acoustic resonator,* Physical review letters **60**, 249 (1988).

[45] A. Otarola, C. De Breuck, T. Travouillon, S. Matsushita, L.-Å. Nyman, A. Wootten, S. J. Radford, M. Sarazin, F. Kerber, and J. P. Pérez-Beaupuits, *Precipitable water vapor, temperature, and wind statistics at sites suitable for mm and submm wavelength astronomy in northern chile,* Publications of the Astronomical Society of the Pacific **131** (2019).

[46] P. F. Goldsmith, I. M. Theory, and T. Society, *Quasioptical systems: Gaussian beam quasioptical propagation and applications* (IEEE press New York, 1998) pp. 141–142.

[47] K. Volk, *Chopping and Nodding for Mid-Infrared Astronomy*, Gemini Observatory (2007).

[48] H. Nyquist, *Thermal agitation of electric charge in conductors,* Physical review **32**, 110 (1928).

[49] A. Pascual Laguna, *Wideband superconducting integrated filter-bank for thz astronomy,* https://eucap.conference2web.com/#!resources/wideband-superconducting-integrated-filter-bank-for-thz-astronomy (2020).

[50] G. Rieke and R. George, *Detection of Light: from the Ultraviolet to the Submillimeter* (Cambridge University Press, 2003) section 2.2 and 2.3.

[51] M. Fox, *Quantum optics: an introduction*, Oxford Master Series in Atomic, Optical and Laser Physics (Oxford Univ. Press, Oxford, 2006) chapter 5 and 6.

[52] G. Marsaglia and J. C. Marsaglia, *A new derivation of stirling's approximation to n!* The American Mathematical Monthly **97**, 826 (1990).

[53] J. Zmuidzinas, *Thermal noise and correlations in photon detection,* Applied optics **42**, 4989 (2003).

[54] T. Takekoshi, K. Karatsu, J. Suzuki, Y. Tamura, T. Oshima, A. Taniguchi, S. Asayama, T. J. Bakx, J. J. Baselmans, S. Bosma, *et al.*, *Deshima on aste: On-sky responsivity calibration of the integrated superconducting spectrometer,* Journal of Low Temperature Physics , 1 (2020).

[55] G. Herbig and R. Zappala, *Near-infrared spectra of nml cygnt and irc+ 10216,* The Astrophysical Journal **162**, L15 (1970).